J. Fluid Mech. (1994), vol. 280, pp. 369–394

Equilibrium dynamics in a forced-dissipative f-plane shallow-water system

By LI YUAN[1]† AND KEVIN HAMILTON[2]

[1]Atmospheric and Oceanic Sciences Program, Princeton University, Princeton, NJ 08542, USA

[2]Geophysical Fluid Dynamics Laboratory/NOAA, Princeton University, Princeton, NJ 08542, USA

(Received 1 March 1994 and in revised form 23 June 1994)

The equilibrium dynamics in a homogeneous forced-dissipative f-plane shallow-water system is investigated through numerical simulations. In addition to classical two-dimensional turbulence, inertio-gravity waves also exist in this system. The dynamics is examined by decomposing the full flow field into a dynamically balanced potential-vortical component and a residual 'free' component. Here the potential-vortical component is defined as part of the flow that satisfies the gradient-wind balance equation and that contains all the linear potential vorticity of the system. The residual component is found to behave very nearly as linear inertio-gravity waves. The forcing employed is a mass and momentum source balanced so that only the large-scale potential-vortical component modes are directly excited. The dissipation is provided by a linear relaxation applied to the large scales and by an eighth-order linear hyperdiffusion. The statistical properties of the potential-vortical component in the fully developed flow were found to be very similar to those of classical two-dimensional turbulence. In particular, the energy spectrum of the potential-vortical component at scales smaller than the forcing is close to the $\sim k^{-3}$ expected for a purely two-dimensional system. Detailed analysis shows that the downscale enstrophy cascade into any wavenumber is dominated by very elongated triads involving interactions with large scales. Although not directly forced, a substantial amount of energy is found in the inertio-gravity modes and interactions among inertio-gravity modes are principally responsible for transferring energy to the small scales. The contribution of the inertio-gravity modes to the flow leads to a shallow tail at the high-wavenumber end of the total energy spectrum. For parameters roughly appropriate for the midlatitude atmosphere (notably Rossby number ~ 0.5), the break between the roughly $\sim k^{-3}$ regime and this shallower regime occurs at scales of a few hundred km. This is similar to the observed mesoscale regime in the atmosphere. The nonlinear interactions among the inertio-gravity modes are extremely broadband in spectral space. The implications of this result for the subgrid-scale closure in the shallow-water model are discussed.

1. Introduction

The study of homogeneous turbulence in two-dimensional, non-divergent flows has been an important area of fluid mechanics over the last quarter-century (e.g.

† Present address: College of Oceanic and Atmospheric Sciences, Oregon State University, Corvallis, Oregon, USA

Kraichnan 1967; Fornberg 1977; Basdevant *et al.* 1981; McWilliams 1984; Legras, Santangelo & Benzi 1988; Maltrud & Vallis 1991). Part of the motivation for these studies has been the belief that the pure two-dimensional model represents an idealized, but still useful, approximation to flow in the atmosphere (e.g. Lilly 1972). The fact that the inviscid, unforced two-dimensional system conserves enstrophy is known to inhibit the transfer of energy to small scales, leading to behaviour very different from that exhibited by three-dimensional homogeneous turbulence. Kraichnan (1967) used theoretical arguments to show that there are two possible inertial ranges for non-divergent homogeneous turbulence: one characterized by a downscale enstrophy cascade (with predicted wavenumber energy spectrum proportional to $\sim k^{-3}$), and one characterized by an upscale energy cascade (with predicted energy spectrum proportional to $\sim k^{-5/3}$). Simulations of the equilibrium spectrum in two-dimensional numerical models have tended to show results in at least qualitative agreement with Kraichnan's theoretical prediction. In particular, at scales smaller than that of the forcing, the simulated energy spectra very roughly approximate $\sim k^{-3}$, although results can depend on the precise characteristics of the forcing and dissipation imposed.

The problem of homogeneous turbulence in a divergent shallow-water model has also been studied recently. This system is of interest as the simplest generalization of the purely two-dimensional model, and for its possible geophysical relevance. In the shallow-water system the enstrophy conservation constraint is relaxed, allowing the possibility of substantial energy transfer to small scales.

An important concept that arises in the analysis and interpretation of the shallow-water model is the division of the flow into a slowly varying 'balanced' component characterized by a diagnostic relation between the pressure and velocity fields, and a high-frequency 'free' component. In the limit of very weak flow the slow component is geostrophic motion, while the high-frequency motions are simply linear inertio-gravity waves. The separation of balanced and free modes in stronger flows is not so straightforward. This issue of defining the balanced and free components is central to many aspects of geophysical fluid dynamics, and the shallow-water model allows this problem to be investigated in its simplest context.

Warn (1986) considered the statistical mechanics of the extremely idealized case of an unforced inviscid rotating shallow-water system. He argued that, even if the initial state is nearly in geostrophic balance, the final statistical equilibrium must be characterized by an equipartition of energy among all modes, including small-scale, high-frequency inertio-gravity waves. Warn used this result to speculate that in the (geophysically relevant) forced-dissipative system geostrophic motions should be similarly unstable, and that the fully developed flow should include significant contributions from the inertio-gravity waves.

Farge & Sadourny (1989, hereafter FS) investigated similar issues through numerical simulation of unforced initial value problems in a rotating shallow-water model with dissipation acting on the smallest resolved scales. They found that, in the parameter range examined (Rossby number $\sim 0.01 - 0.1$ and Froude number $\sim 0.03 - 0.1$), there was little transfer of energy from the balanced modes to inertio-gravity waves. They found significant downscale transfer of energy among the inertio-gravity wave modes, however. Recent papers by Spall & McWilliams (1992) and Polvani *et al.* (1994) have presented further studies of the problem of decaying turbulence in the shallow-water model.

Here we extend the work of FS through detailed analysis of numerical simulations of the equilibrium state of homogeneous turbulence in a forced-dissipative rotating shallow-water model. Part of the motivation for the present study is derived from

observations of the scale dependence of atmospheric motions. Observations of two-dimensional atmospheric energy spectra typically show two distinct power law regimes, one at large scales with slope roughly -3 (e.g. Boer & Shepherd 1983) and another shallower region at scales shorter than about 500 km (e.g. Nastrom & Gage 1985). The nature of the shallow 'mesoscale' spectral regime is controversial. Lilly (1983) regarded this feature of the spectrum as a consequence of a quasi-two-dimensional upscale energy cascade from small-scale convection, accounting for the roughly $\sim k^{-5/3}$ behaviour seen in observations. By contrast, Gage & Nastrom (1986) speculated that the motions in the mesoscale regime may be largely inertia-gravity waves. If Gage & Nastrom are correct, then there may be no need to invoke significant small-scale forcing of atmospheric motions in order to account for the observed mesoscale regime.

An understanding of the interaction of gravity waves and balanced two-dimensional turbulent motions is likely to be crucial for explaining the mesoscale regime of atmospheric flow. Here we will attempt a detailed exploration of these interactions within the simple context of statistically homogeneous flow in the shallow-water model. For the results to be of relevance for the atmosphere it is necessary to extend the parameter range of the flows examined beyond that considered by FS (in particular to flows with Rossby number of order unity).

The outline of this paper is as follows. In §2 we present the basic equations and discuss the technique developed for separating balanced and free components in flows at finite Rossby number. Section 3 begins with a description of the numerical model used in the present simulations. Then the results of the decomposition into the two components are examined along with the basic features of the simulated equilibrium state. The details of the scale interactions in the equilibrium state are diagnosed in §4, and the implications for the parameterization of subgrid-scale motions in numerical models are discussed. Conclusions are given in §5.

2. Decomposition of the potential-vortical and residual components

Consider a plane flat-bottom shallow-water system in a doubly periodic square domain with an unperturbed depth H. The system is rotating about the vertical with a uniform angular velocity $f/2$ where f is the usual Coriolis parameter. Following Lorenz (1980), the governing equations of motion in the absence of forcing and dissipation can be written as

$$\frac{\partial}{\partial t}\nabla^2\psi + J(\psi,\nabla^2\psi) + \nabla\cdot(\nabla^2\psi\nabla\chi) + f\nabla^2\chi + (\bar{u}\nabla^2\psi_x + \bar{v}\nabla^2\psi_y) = 0, \tag{2.1}$$

$$\frac{\partial}{\partial t}\nabla^2\chi + J(\chi,\nabla^2\psi) - \nabla\cdot(\nabla^2\psi\nabla\psi) + \nabla^2(K + gh - f\psi + \bar{u}\psi_y - \bar{v}\psi_x) = 0, \tag{2.2}$$

$$\frac{\partial h}{\partial t} + J(\psi,h) + \nabla\cdot(h\nabla\chi) + H\nabla^2\chi + (\bar{u}h_x + \bar{v}h_y) = 0, \tag{2.3}$$

$$\frac{\partial \bar{u}}{\partial t} - f\bar{v} - \overline{\nabla^2\psi\chi_y} = 0, \tag{2.4}$$

$$\frac{\partial \bar{v}}{\partial t} + f\bar{u} + \overline{\nabla^2\psi\chi_x} = 0, \tag{2.5}$$

with

$$K = (\nabla\psi\cdot\nabla\psi + \nabla\chi\cdot\nabla\chi)/2 + J(\psi,\chi) + (\bar{u}^2 + \bar{v}^2)/2 + (-\bar{u}\psi_y + \bar{v}\psi_x) + (\bar{u}\chi_x + \bar{v}\chi_y), \tag{2.6}$$

where ψ and χ are the streamfunction and velocity potential, h is the surface height departure, and u and v are horizontal velocities. The overbar denotes the horizontal domain average. For completeness, we include the contributions from (as well as prognostic equations for) the domain-averaged velocities $\bar{u}$ and $\bar{v}$ which were ignored by Lorenz. For the parameter range of interest, however, the contribution of the mean velocity terms was found to be negligible, and these terms are dropped from the further development described here. The equation governing the linear potential vorticity ($q = \nabla^2\psi - fh/H$) can be obtained by multiplying (2.3) by $-f/H$ and adding the result to (2.1):

$$\frac{\partial q}{\partial t} + J(\psi, q) + (\chi_x q_x + \chi_y q_y) + q\nabla^2\chi = 0. \tag{2.7}$$

The linearized shallow-water system has eigenmodes belonging to two distinct branches: geostrophically balanced non-divergent zero-frequency motion and inertio-gravity waves with their familiar dispersion relation. FS decomposed their simulated flow fields into geostrophically balanced and inertio-gravity wave components. This approach worked quite well for their decaying turbulence simulations, since the flows were very weak. In the present study, we are interested in flows with larger Rossby and Froude numbers (appropriate for atmospheric conditions), and thus a more accurate decomposition scheme is developed.

Our scheme is based on the use of the gradient-wind approximation for the balanced flow along with the assumption that the balanced motions contain all the linear potential vorticity of the system. This assumption is one of many possible that could be used to relate the divergent and rotational components of the balanced flow. This particular choice is motivated by the nice property that the part of the flow not in the balanced component will have zero linear potential vorticity (which is appropriate for linear inertio-gravity waves). It is ultimately justified *a posteriori* by the results presented below.

We adopt the same terminology as FS and assume the full flow consists of a potential-vortical component (denoted by subscript v) and a residual component (denoted by subscript g):

$$\psi = \psi_v + \psi_g, \tag{2.8}$$

$$\chi = \chi_v + \chi_g, \tag{2.9}$$

$$h = h_v + h_g. \tag{2.10}$$

The potential-vortical component satisfies the gradient-wind balance equation:

$$g\nabla^2 h_v = f\nabla^2\psi_v + 2J(\psi_{vx}, \psi_{vy}) \tag{2.11}$$

and contains all the linear potential vorticity of the system:

$$\begin{aligned} q &= \nabla^2\psi_v - \frac{f}{H}h_v \\ &= \nabla^2\psi_v - \frac{1}{\lambda_o^2}\psi_v + \frac{2}{f\lambda_o^2}\nabla^{-2}J(\psi_{vx}, \psi_{vy}), \end{aligned} \tag{2.12}$$

where $\lambda_o = (gH)^{1/2}/f$ is the Rossby radius of deformation. Here (2.11) has been used to substitute for h_v in deriving (2.12). The gradient-wind balance equation is the approximation to the divergence equation (2.3) obtained by neglecting terms of $O(R^2)$ and higher in the Rossby number expansion. The Rossby number is defined as $R = U/fL$ where U and L are typical velocity and length scales.

To be consistent with the gradient-wind balance equation, the same-order ω-equation is

$$(\nabla^2 - \lambda_o^{-2})\nabla^2\chi_v = \frac{1}{f\lambda_o^2} J(\psi_v, \nabla^2\psi_v). \tag{2.13}$$

Detailed derivations for (2.11) and (2.13) can be found in the literature (see e.g. Spall & McWilliams 1992). Equation (2.12) can be used to invert ψ_v from q diagnostically. Once ψ_v is known, the corresponding h_v and χ_v can be easily calculated by (2.11) and (2.13). The residual fields are then obtained by subtracting the potential-vortical component fields from the full fields.

As a first step to formulating energy equations for the two components, we now derive prognostic equations for the individual variables of both components. Replacing q in (2.7) with a function of ψ_v by (2.12), the prognostic equation for ψ_v can be written as

$$\frac{\partial\psi_v}{\partial t} = (\nabla^2 - \lambda_o^{-2})^{-1}\left(\mathscr{J}_{vv}^{\psi_v} + \mathscr{J}_{vg}^{\psi_v} + \mathscr{J}_{gg}^{\psi_v} - \frac{2}{f\lambda_o^2}\nabla^{-2}\frac{\partial}{\partial t}J(\psi_{vx}, \psi_{vy})\right), \tag{2.14}$$

where

$$\mathscr{J}_{vv}^{\psi_v} = J(\psi_v, q) + (\chi_{vx}q_x + \chi_{vy}q_y) + q\nabla^2\chi_v, \tag{2.15}$$

$$\mathscr{J}_{vg}^{\psi_v} = J(\psi_g, q) + (\chi_{gx}q_x + \chi_{gy}q_y) + q\nabla^2\chi_g, \tag{2.16}$$

$$\mathscr{J}_{gg}^{\psi_v} = 0 \tag{2.17}$$

are the nonlinear terms with subscripts indicating two interacting components and superscripts indicating the equation to which they belong. Note that since $q \equiv q_v$, the subscript v for q has been omitted. Equations (2.15)–(2.17) are obtained by first substituting (2.8) and (2.9) into (2.7) and then grouping all the nonlinear terms together according to the nature of their interacting components. Equation (2.17) states that interactions among modes of the residual component will not generate any potential-vortical component motion.

The prognostic equations for χ_v and h_v can then be derived by taking the time derivative of the ω-equation (2.13) and the gradient-wind equation (2.11) respectively and by substituting $\partial\psi_v/\partial t$ into the resulting equations using (2.14):

$$\frac{\partial\chi_v}{\partial t} = \frac{1}{f\lambda_o^2}\nabla^{-2}(\nabla^2 - \lambda_o^{-2})^{-1}\frac{\partial}{\partial t}J(\psi_v, \nabla^2\psi_v), \tag{2.18}$$

$$\frac{\partial h_v}{\partial t} = -\frac{f}{g}(\nabla^2 - \lambda_o^{-2})^{-1}\left[\mathscr{J}_{vv}^{\psi_v} + \mathscr{J}_{vg}^{\psi_v} + \mathscr{J}_{gg}^{\psi_v} - \frac{2}{f}\frac{\partial}{\partial t}J(\psi_{vx}, \psi_{vy})\right]. \tag{2.19}$$

The interpretation of (2.14), (2.18), and (2.19) is complicated by the appearance of time-derivative terms on the right-hand sides. The contributions of these terms to the energy budgets were evaluated from the numerical simulations described below (see §3.3), and were found to be negligible. For simplicity these time-dependent terms will be neglected in the further development in this section.

Once the prognostic equations for the potential-vortical component are known, the approximate prognostic equations for the residual component can be easily derived by subtracting (2.14), (2.18), and (2.19) from (2.1)–(2.3) respectively:

$$\frac{\partial\psi_g}{\partial t} = \left[-\nabla^{-2}\mathscr{J}_{vv}^{\psi} + (\nabla^2 - \lambda_o^{-2})^{-1}\mathscr{J}_{vv}^{\psi_v}\right] + \left[-\nabla^{-2}\mathscr{J}_{vg}^{\psi} + (\nabla^2 - \lambda_o^{-2})^{-1}\mathscr{J}_{vg}^{\psi_v}\right] + \left[-\nabla^{-2}\mathscr{J}_{gg}^{\psi} + (\nabla^2 - \lambda_o^{-2})^{-1}\mathscr{J}_{gg}^{\psi_v}\right] - f\chi_g, \tag{2.20}$$

$$\frac{\partial \chi_g}{\partial t} = -\nabla^{-2}(\mathscr{J}^{\chi}_{vv} + \mathscr{J}^{\chi}_{vg} + \mathscr{J}^{\chi}_{gg}) - (gh_g - f\psi_g), \tag{2.21}$$

$$\frac{\partial h_g}{\partial t} = \left[\mathscr{J}^{h}_{vv} + (f/g)(\nabla^2 - \lambda_o^{-2})^{-1}\mathscr{J}^{\psi_v}_{vv}\right] + \left[\mathscr{J}^{h}_{vg} + (f/g)(\nabla^2 - \lambda_o^{-2})^{-1}\mathscr{J}^{\psi_v}_{vg}\right] + \left[\mathscr{J}^{h}_{gg} + (f/g)(\nabla^2 - \lambda_o^{-2})^{-1}\mathscr{J}^{\psi_v}_{gg}\right] - H\nabla^2\chi_g. \tag{2.22}$$

Nonlinear terms involving interacting modes of the same components have been grouped together in the square brackets. Those interaction terms with superscripts of full fields are obtained in the same manner as for (2.15)–(2.17). Details are given in Appendix A.

Finally, we derive the energy equations for the two components. The energy spectra are defined here as

$$\hat{E}_V = \frac{1}{2}H(|-\hat{\psi}_{vy} + \hat{\chi}_{vx}|^2 + |\hat{\psi}_{vx} + \hat{\chi}_{vy}|^2) + \frac{1}{2}g|\hat{h}_v|^2, \tag{2.23}$$

$$\hat{E}_g = \frac{1}{2}H(|-\hat{\psi}_{gy} + \hat{\chi}_{gx}|^2 + |\hat{\psi}_{gx} + \hat{\chi}_{gy}|^2) + \frac{1}{2}g|\hat{h}_g|^2, \tag{2.24}$$

where the caret denotes a Fourier space coefficient. In the divergent shallow-water system the true energy is $[(h+H)(u^2+v^2) + gh^2]/2$. This is a cubic quantity, a fact which greatly complicates the analysis (see Warn 1986, for discussion). Following Warn (1986), our definition of energy is a quadratic approximation to the true cubic energy (replacing $H+h$ with H). For all the numerical experiments presented here, the relative differences between the domain-integrated true and approximate energy are less than 1%.

The quadratic energy equations in spectral space are

$$\begin{aligned}
\frac{\partial \hat{E}_V}{\partial t} &= \frac{\partial}{\partial t}\left[\tfrac{1}{2}H(|-\hat{\psi}_{vy} + \hat{\chi}_{vx}|^2 + |\hat{\psi}_{vx} + \hat{\chi}_{vy}|^2) + \tfrac{1}{2}g|\hat{h}_v|^2\right] \\
&= \frac{1}{2}H(k^2 + \lambda_o^{-2})^{-1} \\
&\quad \times \Big|\left[-\hat{\mathscr{J}}^{\psi_v}_{vvy}(-\hat{\psi}^*_{vy} + \hat{\chi}^*_{vx}) + \hat{\mathscr{J}}^{\psi_v}_{vvx}(\hat{\psi}^*_{vx} + \hat{\chi}^*_{vy}) + (f/H)\hat{\mathscr{J}}^{\psi_v}_{vv}\hat{h}^*_v\right] \\
&\quad + \left[-\hat{\mathscr{J}}^{\psi_v}_{vgy}(-\hat{\psi}^*_{vy} + \hat{\chi}^*_{vx}) + \hat{\mathscr{J}}^{\psi_v}_{vgx}(\hat{\psi}^*_{vx} + \hat{\chi}^*_{vy}) + (f/H)\hat{\mathscr{J}}^{\psi_v}_{vg}\hat{h}^*_v\right] \\
&\quad + \left[-\hat{\mathscr{J}}^{\psi_v}_{ggy}(-\hat{\psi}^*_{vy} + \hat{\chi}^*_{vx}) + \hat{\mathscr{J}}^{\psi_v}_{ggx}(\hat{\psi}^*_{vx} + \hat{\chi}^*_{vy}) + (f/H)\hat{\mathscr{J}}^{\psi_v}_{gg}\hat{h}^*_v\right]\Big|,
\end{aligned} \tag{2.25}$$

$$\begin{aligned}
\frac{\partial \hat{E}_g}{\partial t} &= \frac{\partial}{\partial t}\left[\tfrac{1}{2}H(|-\hat{\psi}_{gy} + \hat{\chi}_{gx}|^2 + |\hat{\psi}_{gx} + \hat{\chi}_{gy}|^2) + \tfrac{1}{2}g|\hat{h}_g|^2\right] \\
&= \frac{1}{2}H\Big|\left[(-k^{-2}\hat{\mathscr{J}}^{\psi}_{vvy} + (k^2 + \lambda_o^{-2})^{-1}\hat{\mathscr{J}}^{\psi_v}_{vvy} + k^{-2}\hat{\mathscr{J}}^{\chi}_{vvx})(-\hat{\psi}^*_{gy} + \hat{\chi}^*_{gx})\right. \\
&\quad + (k^{-2}\hat{\mathscr{J}}^{\psi}_{vvx} - (k^2 + \lambda_o^{-2})^{-1}\hat{\mathscr{J}}^{\psi_v}_{vvx} + k^{-2}\hat{\mathscr{J}}^{\chi}_{vvy})(\hat{\psi}^*_{gx} + \hat{\chi}^*_{gy}) \\
&\quad + (g/H)(\hat{\mathscr{J}}^{h}_{vv} - (f/g)(k^2 + \lambda_o^{-2})^{-1}\hat{\mathscr{J}}^{\psi_v}_{vv})\hat{h}^*_g] \\
&\quad + \left[(-k^{-2}\hat{\mathscr{J}}^{\psi}_{vgy} + (k^2 + \lambda_o^{-2})^{-1}\hat{\mathscr{J}}^{\psi_v}_{vgy} + k^{-2}\hat{\mathscr{J}}^{\chi}_{vgx})(-\hat{\psi}^*_{gy} + \hat{\chi}^*_{gx})\right. \\
&\quad + (k^{-2}\hat{\mathscr{J}}^{\psi}_{vgx} - (k^2 + \lambda_o^{-2})^{-1}\hat{\mathscr{J}}^{\psi_v}_{vgx} + k^{-2}\hat{\mathscr{J}}^{\chi}_{vgy})(\hat{\psi}^*_{gx} + \hat{\chi}^*_{gy}) \\
&\quad + (g/H)(\hat{\mathscr{J}}^{h}_{vg} - (f/g)(k^2 + \lambda_o^{-2})^{-1}\hat{\mathscr{J}}^{\psi_v}_{vg})\hat{h}^*_g] \\
&\quad + \left[(-k^{-2}\hat{\mathscr{J}}^{\psi}_{ggy} + (k^2 + \lambda_o^{-2})^{-1}\hat{\mathscr{J}}^{\psi_v}_{ggy} + k^{-2}\hat{\mathscr{J}}^{\chi}_{ggx})(-\hat{\psi}^*_{gy} + \hat{\chi}^*_{gx})\right.
\end{aligned}$$

$$+\left(k^{-2}\hat{\mathscr{F}}^{\psi}_{\mathrm{gg}x}-(k^2+\lambda_\circ^{-2})^{-1}\hat{\mathscr{F}}^{\psi_{\mathrm{v}}}_{\mathrm{gg}x}+k^{-2}\hat{\mathscr{F}}^{\chi}_{\mathrm{gg}y}\right)\left(\hat{\psi}^{*}_{\mathrm{g}x}+\hat{\chi}^{*}_{\mathrm{g}y}\right)$$

$$+(g/H)\left(\hat{\mathscr{F}}^{h}_{\mathrm{gg}}-(f/g)(k^2+\lambda_\circ^{-2})^{-1}\hat{\mathscr{F}}^{\psi_{\mathrm{v}}}_{\mathrm{gg}}\right)\hat{h}^{*}_{\mathrm{g}}\Big]\Big|, \tag{2.26}$$

where a star denotes the complex conjugate. These equations are obtained by taking the following operations respectively:

$$\frac{H}{2}\Big|\left(-(2.14)_y+(2.18)_x\right)\left(-\hat{\psi}^{*}_{\mathrm{v}y}+\hat{\chi}^{*}_{\mathrm{v}x}\right)+\left((2.14)_x+(2.18)_y\right)\left(\hat{\psi}^{*}_{\mathrm{v}x}+\hat{\chi}^{*}_{\mathrm{v}y}\right)+g(2.19)\hat{h}^{*}_{\mathrm{v}}/H\Big|,$$

$$\frac{H}{2}\Big|\left(-(2.20)_y+(2.21)_x\right)\left(-\hat{\psi}^{*}_{\mathrm{g}y}+\hat{\chi}^{*}_{\mathrm{g}x}\right)+\left((2.20)_x+(2.21)_y\right)\left(\hat{\psi}^{*}_{\mathrm{g}x}+\hat{\chi}^{*}_{\mathrm{g}y}\right)+g(2.22)\hat{h}^{*}_{\mathrm{g}}/H\Big|.$$

Energy transfers due to nonlinear interactions involving modes of the same components are grouped together in the square brackets.

3. Numerical experiments and the equilibrium spectrum

3.1. *The numerical model*

A spectral model was used to perform the numerical experiments. The following equations were integrated:

$$\frac{\partial u}{\partial t}+uu_x+vu_y-fv+gh_x=F_u+D_u, \tag{3.1}$$

$$\frac{\partial v}{\partial t}+uv_x+vv_y+fu+gh_y=F_v+D_v, \tag{3.2}$$

$$\frac{\partial h}{\partial t}+(H+h)\nabla\cdot\vec{u}+\vec{u}\cdot\nabla h=F_h+D_h, \tag{3.3}$$

where F and D terms are the forcing and dissipation. Compared with the vorticity and divergence equations, the basic momentum equations have fewer nonlinear calculations; thus it is more convenient and economical to integrate (3.1)–(3.3) than (2.1)–(2.3).

To remove aliasing in the spectral model, nonlinear multiplications are calculated on a transform grid in physical space of dimension $(3N/2+2)\times(3N/2+2)$ where N is the equivalent grid-point model resolution. An explicit leapfrog scheme is used for the time integration. A very weak Robert filter is also applied to remove computational modes. In agreement with the earlier shallow-water model study of Farge & Lacarra (1988) we found that stable integrations required a time-step considerably smaller than that indicated by the CFL criterion.

Most experiments were performed at $N = 256$ (i.e. 128×128 wavenumbers) resolution. The model parameters are chosen to be roughly appropriate for atmospheric motions in midlatitudes. In particular, we chose: the domain size $L = 15.6\times10^6$ m, $H = 100$ m, $g = 10$ m s^{-2}, and $f = 0.4\times10^{-4}$ s^{-1}. The magnitude of the forcing is such that the typical velocities in the fully developed flow are comparable to horizontal winds observed in the atmosphere (and hence are a significant fraction of the 31 m s^{-1} linear gravity wave phase speed in the model). The time-step size is 180 s. Results will be discussed in terms of wavevectors and wavenumbers non-dimensionalized by the domain size.

The model is forced at large scales by injecting random momentum and mass sources balanced so that they directly excite only the potential-vortical component. This is to represent the generation of large-scale atmospheric eddy motions (which is thought to occur largely though instability processes that are essentially quasi-

geostrophic). Implementation of this forcing begins with the generation of a scale-selective, random Markovian streamfunction defined in spectral space as

$$\hat{\psi}_n = \hat{\psi}_\circ(1-\alpha^2)^{1/2}e^{i\theta} + \alpha\hat{\psi}_{n-1}, \tag{3.4}$$

where $\hat{\psi}_\circ$ is a wavenumber-dependent forcing amplitude (non-zero only for wavenumbers with magnitude between 7 and 9), θ is a random number varying from 0 to π for each two-dimensional wavevector. The subscript notation denotes that the nth version of the streamfunction is generated from the $n-1$st. The factor α (<1) is the correlation coefficient between successive versions. (This is the same functional form as that used by Maltrud & Vallis 1991, for their two-dimensional turbulence studies.) Next, the corresponding height and velocity potential forcing fields are calculated from the streamfunction using (2.11) and (2.13) respectively. These height and velocity fields are then used to determine the momentum and mass forcing applied to the governing equations (3.1)–(3.3). Here $\alpha = 0.5$ is chosen and at every 10 time-steps (1800 s) a new $\hat{\psi}_n$ is generated. Maltrud & Vallis (1991) found some sensitivity of their non-divergent model results to the choice of the time correlation of their forcing. The addition of the divergent flow in the present model raises the possibility of further sensitivity. While the forcing is designed to directly excite only balanced motions, decreasing α will produce more high-frequency unsteadiness in the flow which might be expected to enhance the transfer of energy into the residual component. In fact the results from the experiments reported here have been found to be not strongly sensitive to the value of α. As a final point concerning the forcing, note that the Rossby radius of deformation is about $L/3$, i.e. somewhat larger than the forcing scale.

The dissipation consists of a linear relaxation and a ∇^8 linear diffusion acting on both the velocity and height fields. The linear relaxation is applied only to modes with wavenumber less than 6. The large-scale linear drag has timescale of 4.32×10^6 s (50 days), and the coefficient for the diffusion is 10^{29} m^8 s^{-1} (resulting in a dissipation timescale of about 2 days for wavenumber 128).

The model was integrated from rest. After about 200 days the secular increase in domain-integrated enstrophy and energy ceased. In the experiments reported here, the first 400 days of integration are discarded and the statistics are computed on the basis of 500 instantaneous model fields sampled during the next 100 days (unless otherwise noted).

3.2. *Results of application of decomposition procedure*

The actual application of the decomposition procedure to the model output begins with the computation of the linear potential vorticity from the full instantaneous fields. Then the potential-vortical component streamfunction is obtained diagnostically by inverting the linear potential vorticity from (2.12) using an iterative method. The iteration starts by ignoring the nonlinear term, thus the initial guess uses the pure geostrophic approximation. Then this geostrophically balanced field is used to approximate the nonlinear term. Treating the nonlinear term as known, the equation is then linear for the next guess streamfunction and can be easily inverted again. This process can be repeated until the convergence is reached. The potential-vortical height and velocity potential can then be calculated by straightforward inversion of (2.11) and (2.13).

Figure 1 shows the result of a single iteration of the decomposition procedure (i.e. geostrophic balance). Displayed are the vorticity computed from the potential-vortical component (*a*) and the residual component (*b*). For clarity of presentation only a portion of the domain is shown. This is an instantaneous sample taken after

the spin-up period. The Rossby number (computed as the mean absolute value of relative vorticity divided by f) is about 0.45, and the root-mean-square velocity and surface height are about 8 m s^{-1} and 9 m respectively (Froude number about 0.25). Inspection of figure 1 reveals regions of strong negative vorticity in the residual component that are highly correlated with locations of anticyclones in the potential-vortical component. Since the residual component does not contain any linear potential vorticity, its vorticity field is proportional to its height field ($\nabla^2\psi_g = fh_g/H$). These strong 'lows' in the residual component result from the potential-vortical component anticyclone highs being overestimated by the simple geostrophic balance. The same effect exists for cyclones: the geostrophic balance underestimates lows in cyclonic circulations resulting some strong 'highs' in the residual component. Figure 2 shows the same vorticity fields, but after three iterations to approximate the full gradient-wind balance. The apparently unrealistic features in the residual component are greatly reduced. No noticeable improvement occurs with further iterations. There is no theory that predicts how fast this iterative method will converge, or if it must converge at all. From our test results, however, it seems three iterations are sufficient to effectively separate the two components. Thus we will employ three iterations in all calculations presented below.

The effectiveness of the decomposition procedure is further analysed by computation of the space–time spectrum of the potential-vortical and residual components of the flow. In this calculation (and in all other spectral calculations reported here) the two-dimensional wavenumber spectrum has been integrated along circles in the two-dimensional wavevector space to obtain the one-dimensional spectrum. Only the part of the spectrum for wavenumbers $\leqslant N/2$ is plotted. (Note that some of the calculations described here have been repeated with a 'circular truncation' in which the amplitudes for modes with wavenumber $\leqslant N/2$ are set to zero at each time-step. The results for the wavenumber range $\leqslant N/2$ are not much affected if either the square or circular truncation is employed.)

Figure 3 (*a–c*) shows contour plots of space–time spectra of the total energy, the potential-vortical component energy, and the residual component energy, based on five days of integration after the spin-up period in an experiment with the standard ($N = 256$) model. During this particular 5 day segment the forcing and dissipation were set to zero, in order to closely approximate a free system. A time series consisting of 240 instantaneous samples at 10 time-step (30 minutes) intervals was used to calculate the spectra. Practical considerations limited the length of the time series that could be used to calculate the spectra. This time series is not long enough to capture very low-frequency motions, thus a data tapering window of split-cosine bell shape (with $\sim 8\%$ tapering) has been applied in the time domain. This is designed to suppress the artificial leakage of low-frequency modes to higher frequencies. However, as a side effect, the data tapering introduces spurious oscillations in the computed spectra (this accounts for the isolated maxima at low wavenumber that appear up the frequency axis in figure 3). Nevertheless, when compared with untapered spectra (not shown), the contamination by the leakage has been greatly reduced. For reference the heavy solid curve in panel (*c*) shows the inertio-gravity wave dispersion relation, $\omega^2 = f^2 + c^2k^2$, where ω is the wave frequency and $c = (gH)^{1/2}$.

It is clear that the energy concentrated at large scales and low frequencies in figure 3(*a*) is largely associated with the potential-vortical component, while the energy concentrated along the linear inertio-gravity wave dispersion relation curve is mostly from the residual component. This indicates that the residual component does indeed behave like linear inertio-gravity waves. The energy in the residual component

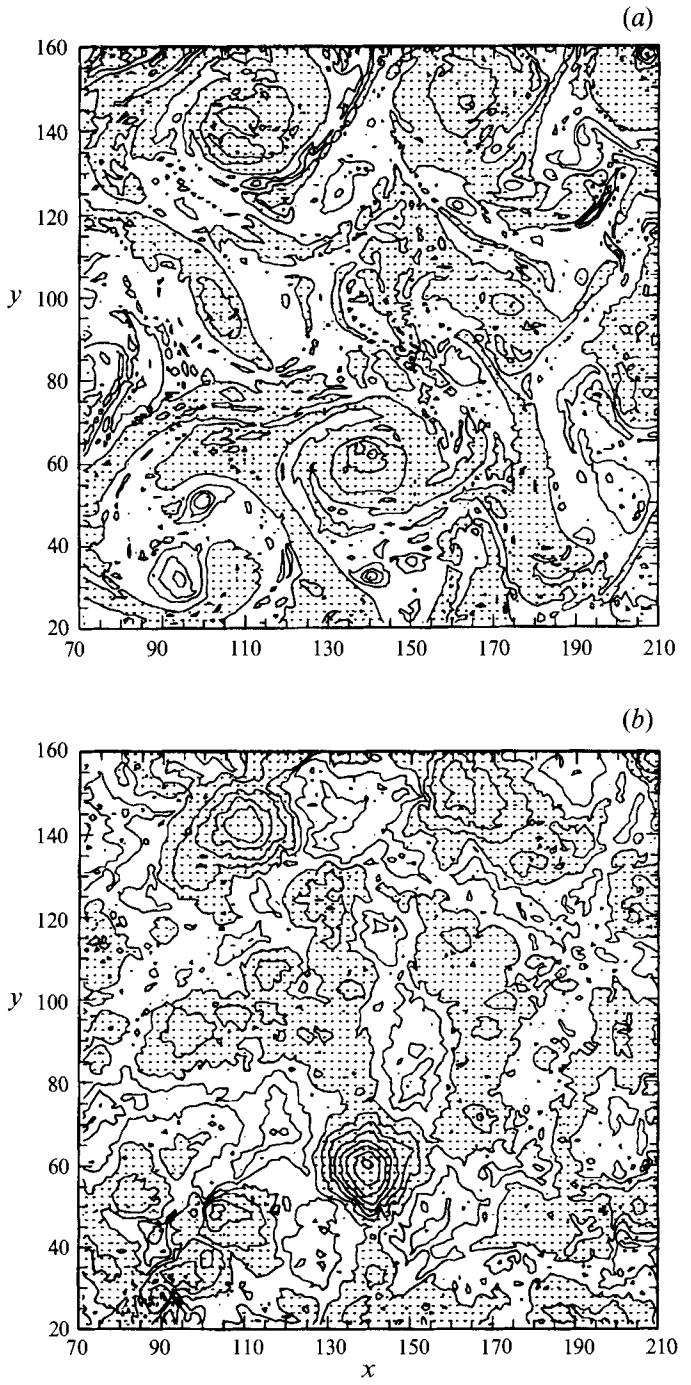

FIGURE 1. Vorticity fields of the two components for the initial guess in the separation procedure. The labelling on the x- and y-axes refer to grid-points in the equivalent 256×256 physical space grid. (*a*) The potential-vortical component with contour interval of 3.0×10^{-5} s^{-1} and (*b*) the residual component with contour interval of 1.6×10^{-6} s^{-1}. Negative values are shaded.

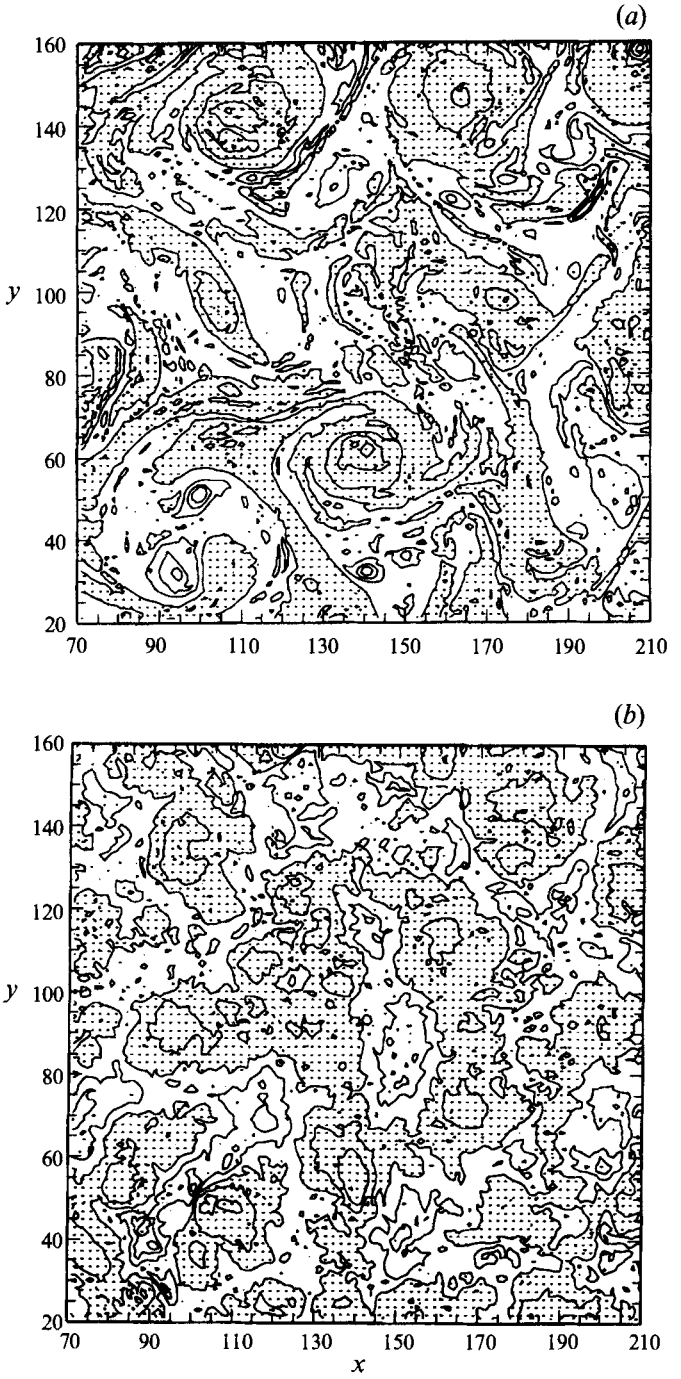

FIGURE 2. As in figure 1, but after three iterations.

is spread in a region around the linear dispersion relation, of course (figure 3*c*). This is presumably due to Doppler shifting effects. The two dashed curves plotted are the frequency shifting limits obtained using the root-mean-square velocity of 8 m s^{-1}. At each wavenumber, the spectral energy density drops about a decade from the peak to the shifting limits. There is some weak concentration of potential-vortical energy

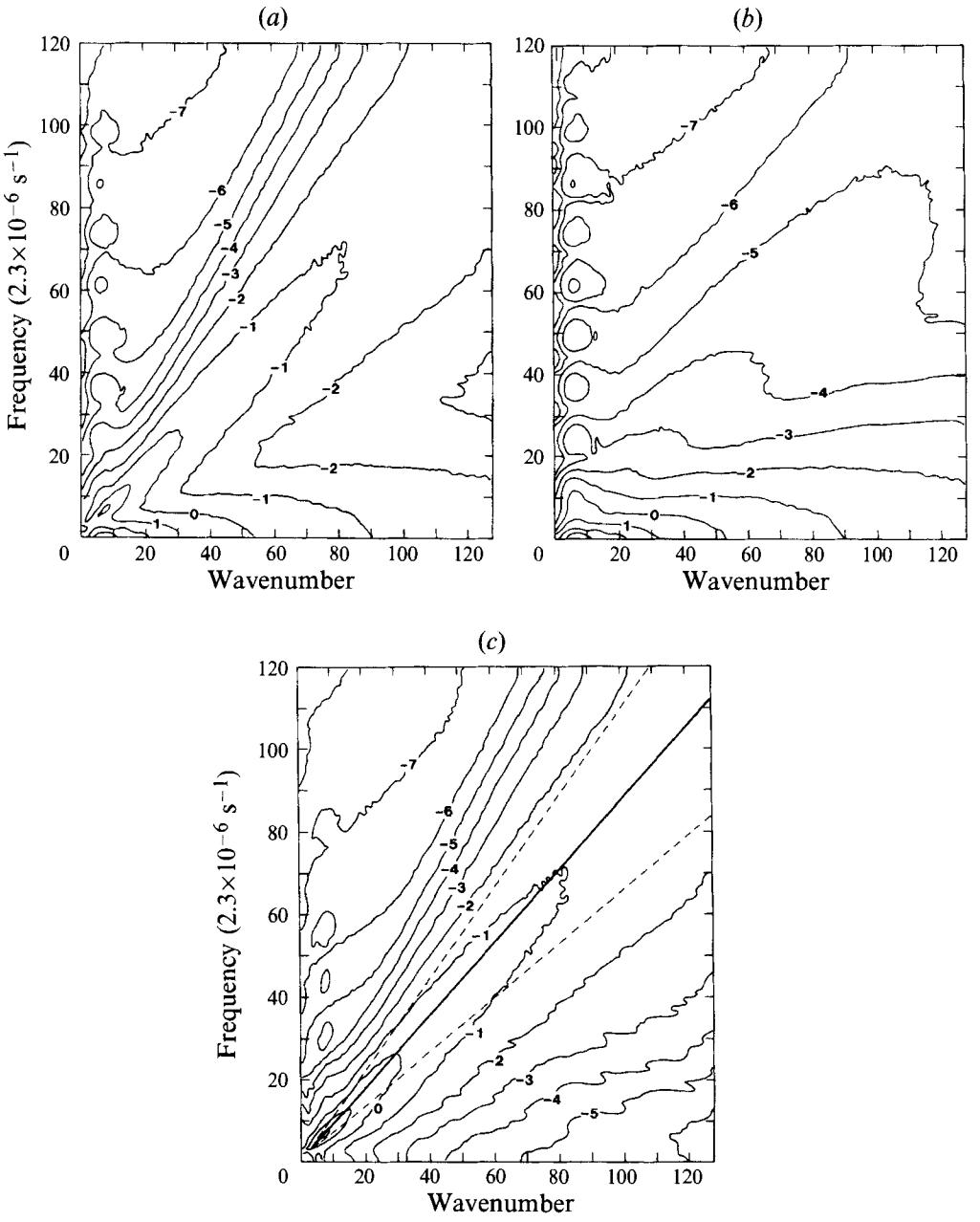

FIGURE 3. Space–time energy spectra (*a*) for the total energy, (*b*) for the potential-vortical component energy, and (*c*) for the residual component. The contours are base-10 logarithmic values and zero corresponds to 10^{20} m^3 s^{-1}. In (*c*), the solid curve is the dispersion relation for linear inertio-gravity waves, while the two dashed curves represent the Doppler shifting limits. See text for details.

along the inertio-gravity dispersion curve (figure 3*b*). This is presumably a measure of the inaccuracy in the present decomposition scheme. It is very encouraging that the energy density in this part of the potential-vortical component spectrum is about 3 to 4 orders of magnitude smaller than that of the residual component in same regions.

The decomposition scheme proposed here is apparently quite effective in separating

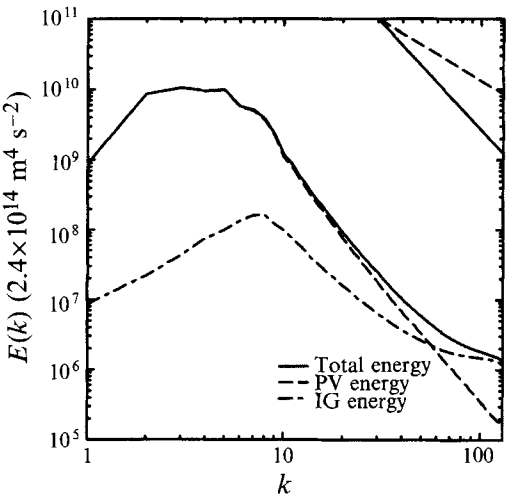

FIGURE 4. Statistical equilibrium energy spectra. Plotted for reference in the upper right corner in this and subsequent plots are two straight lines with slopes of -3 (solid) and $-5/3$ (dashed).

the full flow fields into a slowly varying dynamically balanced component and a residual component that has properties very similar to linear inertio-gravity waves. It is striking that this works so well even at fairly high Rossby and Froude numbers. Henceforth, the residual field that emerges from the decomposition will be referred to simply as the inertio-gravity wave component.

3.3. *Equilibrium spectra*

Now we examine the equilibrium spectrum of the shallow-water model in more detail. Figure 4 shows energy spectra of the total field, the potential-vortical component, and the inertio-gravity wave component for the standard model integration. For $k < 10$, the total energy is mainly in the potential-vortical component and peaks at a wavenumber slightly below the forcing range (7–9). The drop in energy at very small wavenumbers presumably is a consequence of the linear relaxation applied at these scales. For $k > 10$, the potential-vortical component energy spectrum approximates a power law, but with a slight shallowing of the slope at higher wavenumbers. In order to characterize this more precisely, we performed a least-squares fit to the spectrum in the subjectively chosen regions $10 < k < 30$ and $30 < k < 128$. For $10 < k < 30$ the spectrum behaves as roughly $\sim k^{-3.8}$, while for $30 < k < 128$ it approximates $\sim k^{-3.3}$. The inertio-gravity wave component spectrum peaks at wavenumber ~ 8 and it clearly is not close to any simple power law. Overall, it is shallower than the potential-vortical component spectrum (except at the low-wavenumber end), and (for this particular experiment) it eventually crosses the potential-vortical spectrum at wavenumber ~ 61.

High-resolution numerical simulations of two-dimensional turbulence typically produce spectra with slopes steeper than -3 in the enstrophy inertial range (e.g. Fornberg 1977; Basdevant *et al.* 1981; McWilliams 1984), generally a symptom that the flow includes long-lived spatially coherent structures. One possible measure of the degree of this intermittency is the vorticity kurtosis $(\overline{\zeta^4}/\overline{\zeta^2}^2)$ which would have a value of 3 for a Gaussian random field (e.g. Maltrud & Vallis 1991). For this shallow-water model experiment, the vorticity kurtosis (calculated only with the potential-vortical

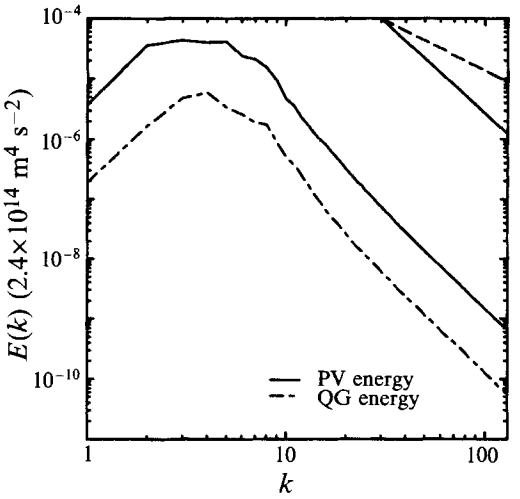

FIGURE 5. Energy spectra of the quasi-geostrophic and shallow-water models when run with identical forcing and dissipation. The quasi-geostrophic spectrum has been shifted downward by one decade. Only the energy in the potential-vortical component has been considered in the shallow-water model result.

component vorticity) during the statistical equilibrium stage is about 6, demonstrating at least some degree of coherent structure in the flow.

As part of the present project, a purely quasi-geostrophic one-layer numerical spectral model was also constructed (see Yuan 1993, for details). The parameters and forcing for this model were taken to be as similar as possible to that for the full primitive equation shallow-water model. Figure 5 compares the energy spectrum for this quasi-geostrophic model with that of the potential-vortical component in the shallow-water model (identical to that shown in figure 4). At wavenumbers greater than those of the forcing (i.e. $k > 9$) the spectra are almost identical (differences at very low wavenumber presumably reflect sampling errors). The vorticity kurtosis for the quasi-geostrophic model experiment is about 6.5, only slightly larger than that of the shallow-water model. Thus there is little indication of strong impact of the inertio-gravity waves on the dynamics of the balanced component of the flow (even at the reasonably large Rossby number in this simulation).

Energy transfer rates due to nonlinear interactions were explicitly calculated in order to examine the maintenance of the statistical equilibrium. Dividing the energy equations (2.25) and (2.26) by $\hat{E}_V(\boldsymbol{k})$ and $\hat{E}_g(\boldsymbol{k})$ respectively, terms on the right-hand sides of the resulting equations are the transfer rates in the two-dimensional spectral space. These two-dimensional transfer rates are then averaged along circular wavenumber bands to obtain one-dimensional transfer rates. Figure 6 shows the results (averaged over the same 100 day period as the power spectra discussed earlier). The balance for the potential-vortical component is relatively simple (figure 6*a*). Forcing puts energy into the system directly in the forcing wavenumber range ($7 \leqslant k \leqslant 9$). This injected energy is transferred to both lower and higher wavenumbers by nonlinear interactions within potential-vortical modes (vv interactions), and then is removed by dissipation. Nonlinear interactions between modes of the two components (vg interactions) make virtually no contribution to the transfer of the potential-vortical component energy.

The inertio-gravity waves are not directly forced (figure 6*b*). For $k > 10$ energy

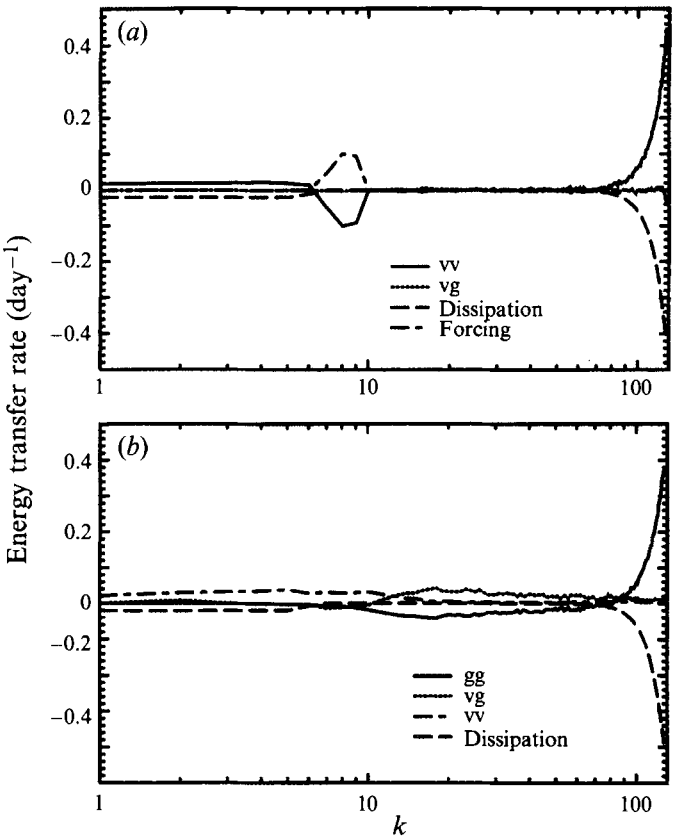

FIGURE 6. The energy transfer rates (*a*) for the potential-vortical component, and (*b*) for the inertio-gravity component.

is input to the inertio-gravity modes by interactions between modes of the two components (vg interactions). Nonlinear interactions among the inertio-gravity waves (gg interactions) transfer the converted energy to the dissipation ranges at large and small wavenumbers (mostly to the high wavenumbers). The interactions between potential-vortical modes (vv interactions) also convert some energy to the inertio-gravity waves, but mostly in the low-wavenumber range.

The sensitivity of the equilibrium spectra to the forcing amplitude and rotation rate parameters have been examined. Shown in figure 7 are the equilibrium energy spectra for two experiments, one with all parameters the same as the standard case but with half the forcing amplitude, and one with all parameters the same as the standard case but with half the rotation rate. The Rossby number for the first experiment is 0.26, while that for the second is 0.8. The shape of the potential-vortical spectrum in both of these experiments is virtually the same, but the inertio-gravity component spectrum is clearly greatly affected by varying these two parameters. When examined in conjunction with figure 5, the results in figure 7 show that the residual component spectrum becomes shallower as the Rossby number increases. Further sensitivity experiments were carried out by varying these two parameters (not shown). The inertio-gravity energy is found to be less than that of the potential-vortical mode at all resolved wavenumbers (i.e. up to $k = 128$) whenever the Rossby number is less than 0.2.

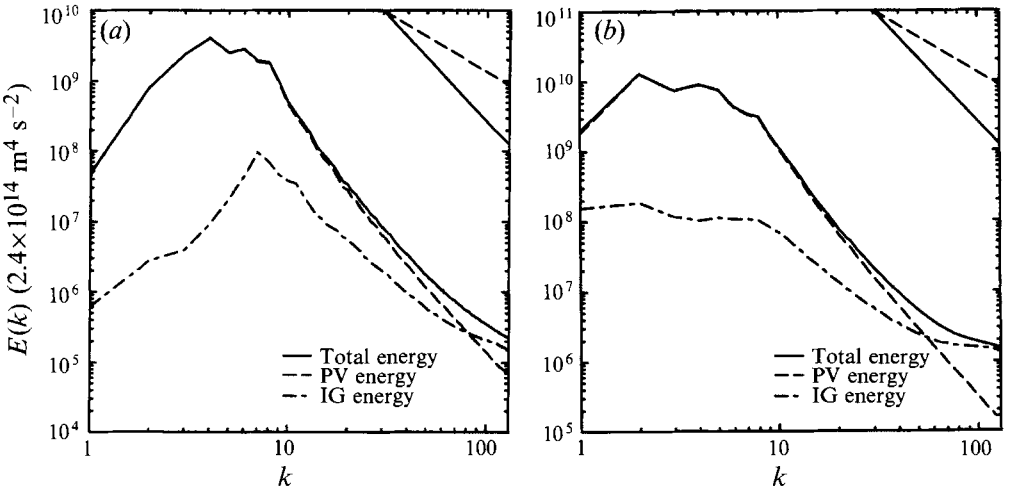

FIGURE 7. Energy spectra for an experiment with (*a*) half the forcing, and (*b*) half the rotation rate of the standard experiment (results plotted in figure 4).

4. Characteristics of the scale interactions: implications for subgrid-scale parameterization

4.1. *Spectral decomposition of vv interactions and gg interactions*

The energy transfer rates defined in the energy equations of (2.25) and (2.26) are the sums of contributions of all possible triad interactions. Each triad consists of two components in the nonlinear interaction function and one component of the velocity or height field. Here we determine the dominant triads contributing to the energy balance at any wavenumber. For example, in spectral space the vv interaction of (2.15) can be expressed as

$$\begin{aligned}\hat{\mathscr{F}}^{\psi v}_{vv}(\boldsymbol{k}) &= \sum_{\boldsymbol{l}} f_q(\boldsymbol{l}) \\ &= \sum_{\boldsymbol{l}} \hat{q}_x(\boldsymbol{l})(\hat{\chi}_{vx}(\boldsymbol{k}-\boldsymbol{l}) - \hat{\psi}_{vy}(\boldsymbol{k}-\boldsymbol{l})) \\ &\quad +\hat{q}_y(\boldsymbol{l})(\hat{\chi}_{vy}(\boldsymbol{k}-\boldsymbol{l}) + \hat{\psi}_{vx}(\boldsymbol{k}-\boldsymbol{l})) + \hat{q}(\boldsymbol{l})(\hat{\chi}_{vxx}(\boldsymbol{k}-\boldsymbol{l}) + \hat{\chi}_{vyy}(\boldsymbol{k}-\boldsymbol{l})) \quad (4.1)\end{aligned}$$

or equivalently as

$$\begin{aligned}&= \sum_{\boldsymbol{l}} f_u(\boldsymbol{l}) \\ &= \sum_{\boldsymbol{l}} (\hat{\chi}_{vx}(\boldsymbol{l}) - \hat{\psi}_{vy}(\boldsymbol{l}))\hat{q}_x(\boldsymbol{k}-\boldsymbol{l}) \\ &\quad +(\hat{\chi}_{vy}(\boldsymbol{l}) + \hat{\psi}_{vx}(\boldsymbol{l}))\hat{q}_y(\boldsymbol{k}-\boldsymbol{l}) + (\hat{\chi}_{vxx}(\boldsymbol{l}) + \hat{\chi}_{vyy}(\boldsymbol{l}))\hat{q}(\boldsymbol{k}-\boldsymbol{l}), \quad (4.2)\end{aligned}$$

where $\boldsymbol{k}$ and $\boldsymbol{l}$ are wavevectors. Then $f_q(\boldsymbol{l})$ represents the contributions to $\hat{\mathscr{F}}^{\psi v}_{vv}$ at wavevector $\boldsymbol{k}$ from the the interaction of a field related to potential vorticity at wavevector $\boldsymbol{l}$ and a field related to velocity at wavevector $(\boldsymbol{k}-\boldsymbol{l})$. Similarly, $f_u(\boldsymbol{l})$ represents the contributions from the field related to velocity at $\boldsymbol{l}$ interacting with the field related to potential vorticity at $(\boldsymbol{k}-\boldsymbol{l})$. The interpretation of f_q and f_u is complicated since the potential vorticity itself is a function of the velocity. For any particular wavevector of interest $(\boldsymbol{k})$, terms formed by $f_q(\boldsymbol{l})$ or $f_u(\boldsymbol{l})$ multiplied by

$-\hat{\psi}^*_{vy}(k) + \hat{\chi}^*_{vx}(k)$ are proportional to the potential-vortical component energy transfer rates (see (2.25)).

This technique is applied to analyse the vv interaction in the potential-vortical component. It may be more meaningful to express this nonlinear interaction in terms of enstrophy transfer rates. The enstrophy equation in spectral space can be obtained easily by rewriting (2.14) in the spectral space and multiplying both sides of the resulting equation with $(k^2 + \lambda_o^{-2})^{-1}\hat{q}^*(\boldsymbol{k})/|q(\boldsymbol{k})|^2$. Thus $f_q(\boldsymbol{l})$ and $f_u(\boldsymbol{l})$ multiplied by $(k^2 + \lambda_o^{-2})^{-1}\hat{q}^*(\boldsymbol{k})/|q(\boldsymbol{k})|^2$ are the two-dimensional enstrophy transfer rates. Note that for any wavevector of interest ($\boldsymbol{k}$), this multiplier is a constant to $f_q(\boldsymbol{l})$ or $f_u(\boldsymbol{l})$ for all wavevectors $\boldsymbol{l}$. In order to obtain better statistics, such decomposition calculations are repeated for all modes with wavevectors within a narrow circular wavenumber band and the results are averaged.

Figure 8 shows the decomposition of vv interaction in transferring enstrophy of modes within two arbitrarily chosen bands in the high-wavenumber range, $38 \leqslant k \leqslant 40$ and $58 \leqslant k \leqslant 60$. These calculations were performed on results from an $N = 160$ model resolution run with parameters similar to the standard experiment described in §3 (although with the diffusion coefficient increased). The results in figure 8 represent the average of 200 instantaneous samples after the spin-up period. It is clear from this figure that the main contributions to enstrophy transfer come from interactions of a few modes of similar scales (dashed curves) with quite large-scale modes (solid curves). Through this interaction, modes in each band gain enstrophy from wavevectors with about 8 lower adjacent wavenumber modes and lose enstrophy to about 8 higher adjacent wavenumber modes. From the limited analysis conducted here the spread of the interaction in spectral space (measured by the width of the peaks and troughs in the dashed curves in figure 8) appears to be independent of the wavenumber considered. At this point we have no clear idea of what determines the degree of this spread.

This result is broadly consistent with the notion of a forward (downscale) enstrophy cascade, in that the positive enstrophy flux into any wavenumber depends only on interactions with smaller wavenumber modes. The details of the scale dependence of the interactions in the enstrophy casacade intertial range have been debated by earlier workers (e.g. Kraichnan 1975; Pouquet *et al.* 1975; Basdevant *et al.* 1981; Hoyer & Sadourney 1982). The most intuitive picture of the physics of an inertial range cascade would suggest that the significant interactions should involve only spectral components of very similar scale (i.e. the triad wavevectors should form a nearly equilateral triangle). This may be the case for the two-dimensional reverse energy cascade (e.g. Hoyer & Sadourney 1982). On the other hand, given the very steep spectrum in the forward entrophy cascade range it may be reasonable to expect the dominant nonlinear transfers to involve the large scales, and this has been the basis of earlier phenomenological models of the turbulence within this regime (e.g. Basdevant, Lesieur & Sadourny 1978; Hoyer & Sadourny 1982). Basdevant *et al.* (1981) argued that this 'non-local' interaction should dominate in the case of purely nonintermittant turbulence, but that any intermittant behaviour restores the spectral locality of the interactions.

Recently Ohkitani & Kida (1992) and Maltrud & Vallis (1993) have used direct numerical simulations with the purely non-divergent system to investigate this problem. They arrive at essentially the same conlcusion as resulted from the present analysis of the shallow-water model (e.g. figure 2 of Maltrud & Vallis 1993 is directly comparable to the present figure 8).

The present results are a confirmation of the spectral 'non-locality' of the inter-

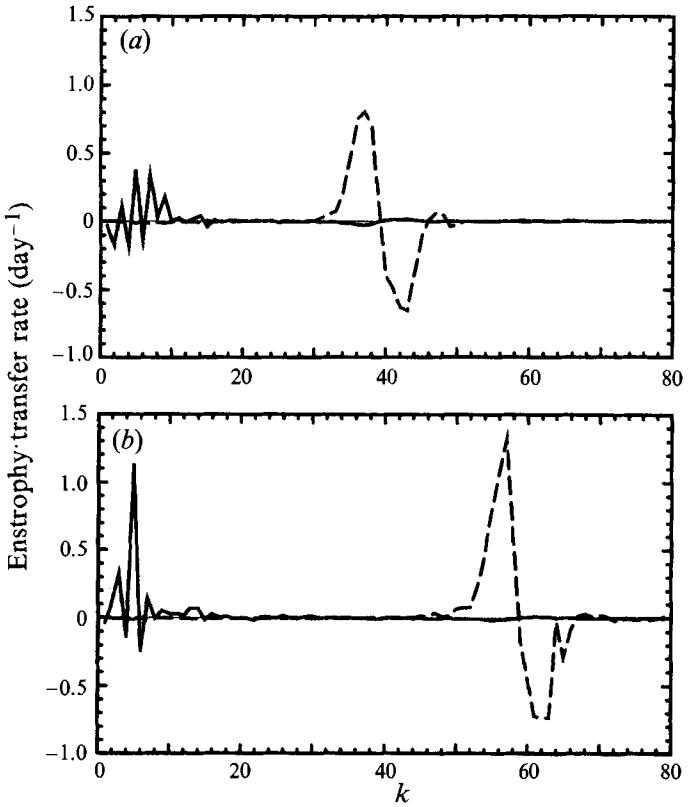

FIGURE 8. Decomposition of the vv interaction contribution to enstrophy transfer (i.e. enstrophy transfer among the potential-vortical component modes). The solid and dashed curves are for f_q and f_u respectively. See text for details.

actions in the forward cascade, even in the presence of some intermittency. The dominant triads in the enstrophy cascade are very elongated. In physical space then, the forward turbulent enstrophy cascade in the potential-vortical component of the present shallow-water model is apparently largely a consequence of distortion of local potential vorticity by the large-scale flow field.

We can use the same approach to decompose all the gg interactions in the inertio-gravity wave energy equation (2.26). Since there are many terms involved in the interaction functions, the two interacting components are arbitrarily assigned as $f_a(l)$ and $f_b(l)$ (see Appendix B). Figure 9 shows the transfer rates calculated from $f_a(l)$ and $f_b(l)$ for gg interactions contributing to the $38 \leqslant k \leqslant 40$ and $58 \leqslant k \leqslant 60$ bands. The extremely broadband nature of the spectral energy transfers is clear. The inertio-gravity wave modes in each band gain energy from all modes of larger scales and lose to all modes of smaller scales through these gg interactions.

4.2. *Sensitivity to model resolution*

The difference in the nature of vv and gg interactions is reflected in the sensitivity of the potential-vortical and inertio-gravity component spectra to the model resolution. This is demonstrated in figure 10 where the equilibrium spectra obtained with three model resolutions (N = 160, 256, and 432) are plotted. Forcing parameters are selected so that the system is equally (in the statistical sense) forced in each case. The

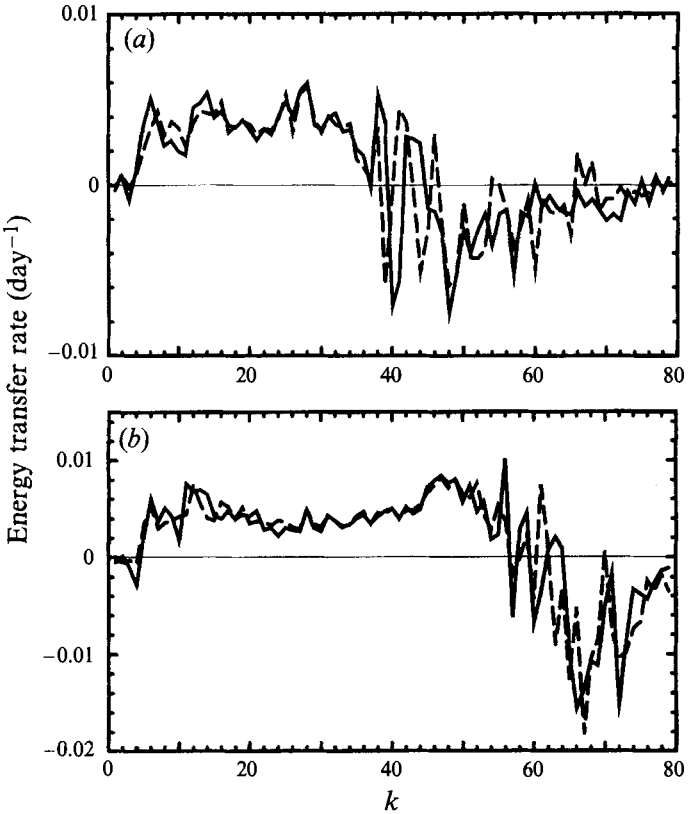

FIGURE 9. Decomposition of gg interaction for the inertio-gravity component energy transfer. The solid and dashed curves are for f_a and f_b respectively. (*a*) $38 \leqslant k \leqslant 40$, and (*b*) $58 \leqslant k \leqslant 60$.

∇^8 diffusion coefficient is also adjusted according to

$$\nu_1^8 k_{1\max}^8 = \nu_2^8 k_{2\max}^8, \tag{4.3}$$

where $k_{\max} = k_{N/2+1}$ is the highest resolved wavenumber. For non-divergent models this is the obvious choice for scaling the dissipation, since it ensures that the timescale for enstrophy dissipation at the smallest resolved scale will be independent of resolution. The present shallow-water model the results in figure 10(*a*) show that this scaling of dissipation does indeed produce an inertial range in the potential-vortical component that is insensitive to the model resolution. The spectrum simply extends to higher-wavenumber ranges with the same slope when model resolution increases. By contrast, the inertio-gravity wave component spectrum (figure 10*b*) is highly sensitive to the model resolution. The lower the model resolution, the shallower is the slope of the inertio-gravity wave energy spectrum (at least for wavenumbers greater than about 10). At the low-wavenumber end the effect of resolution is apparently even more complicated, with the minimum values actually occurring at the intermediate resolution.

The basic features of these results may be understood in the light of the contrasting nature of the vv and gg nonlinear interactions. Since only a limited number of modes are involved in cascading the enstrophy, any mode in the inertial range should not significantly feel the effects of modes with significantly smaller scales (figure 9). As long as the subgrid-scale parameterization scheme (∇^8 diffusion) provides the same rate of enstrophy dissipation at the high-wavenumber end, the effect of subgrid-scale

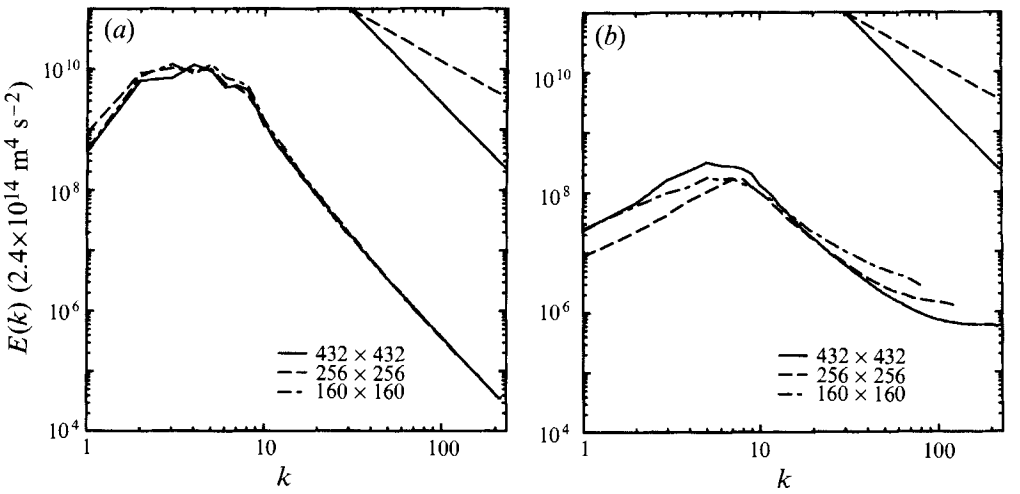

FIGURE 10. Energy spectra for shallow-water model integrations at three spatial resolutions, (*a*) for the potential-vortical component and (*b*) for the residual component.

potential-vortical component modes is apparently well parameterized. In contrast, the gg interactions transfer significant energy from any wavenumber to modes of all smaller scales. When the model resolution is reduced, fewer smaller-scale modes are available as a sink. The ∇^8 diffusion dissipates only a very limited number of highest-wavenumber modes: lower-wavenumber modes cannot feel subgrid-scale inertio-gravity wave effects through this parameterization.

The result in figure 10(*b*) shows the difficulty in formulating an acceptable subgrid-scale parameterization even for the simple case of homogeneous turbulence in a shallow-water model. It seems likely that any formulation that can produce inertio-gravity component spectra independent of resolution must depend nonlinearly on the flow. The implications of this conclusion may be significant for global three-dimensional atmospheric simulation models, particularly as the resolution increases to the point where a portion of the mesoscale regime can be represented (e.g. Strahan & Mahlman 1994).

4.3. *Spectral decomposition of vg interaction and the source of inertio-gravity waves*

The results in figure 6(*b*) show that inertio-gravity waves of all scales gain energy though vg interactions. In this section we show the results of a scale decomposition of the vg interactions. All terms involved in vg interactions in the energy equation (2.26) are represented as the sum of triads in a manner analogous to that in (4.1). The two interacting components are assigned such that $f_v(l)$ and $f_g(l)$ depend on the potential-vortical component fields and inertio-gravity component fields, respectively. The algebra involved in deriving the expressions for these two functions is straightforward, but very lengthy (see Yuan 1993, for details). The results are shown in figure 11 for the same two wavenumber bands used in the earlier discussion of vv and gg interactions. It is clear that for both wavenumber bands, the energy transfer results from the interactions with the large-scale potential-vortical component modes. In that sense, we can regard the inertio-gravity waves as being generated by the instability of the large-scale potential-vortical component modes. Small-scale inertio-gravity modes are apparently nearly decoupled from the small-scale potential-vortical modes. The fact that interactions are dominated by one one small-wavenumber potential-

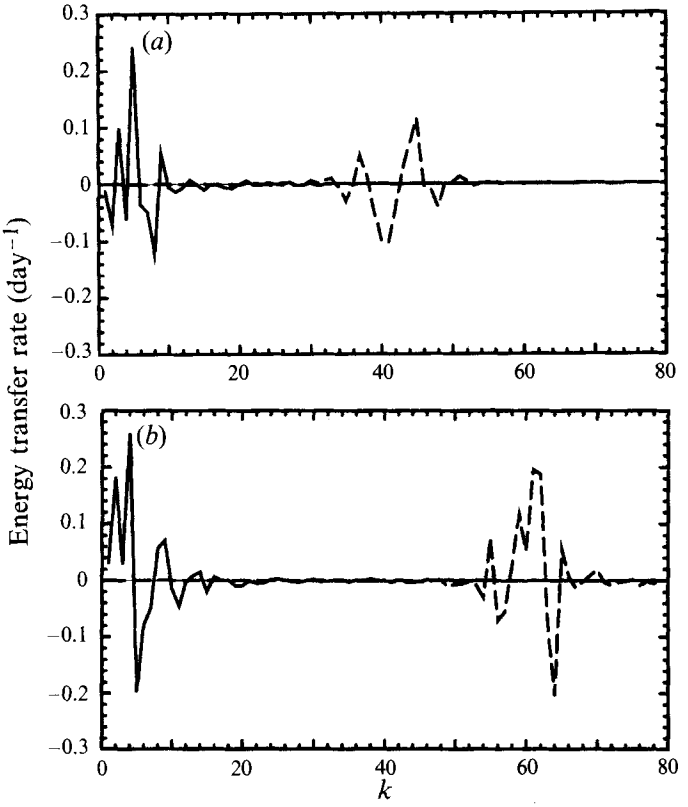

FIGURE 11. As in figure 9, but for vg interaction (i.e. the inertio-gravity component energy transfer). The solid and dashed curves are for f_v and f_g respectively.

vortical mode and two large-wavenumber inertio-gravity modes is reasonable, since the small frequency difference between the inertio-gravity modes could be close to the (presumably very small) frequency for the potential-vortical mode.

To investigate further the generation of gravity waves, we have also calculated the divergence of inertio-gravity wave energy fluxes, $\nabla \cdot (h_g \boldsymbol{u}_g)$, in physical space. In figure 12 this divergence is plotted together with the potential-vortical component vorticity field. These results are for a 5 day average of the $N = 256$ model resolution standard experiment. In these figures, the absolute value of potential-vortical component vorticity is plotted since we do not distinguish cyclonic and anticyclonic motions for this purpose. Only the positive values of inertio-gravity wave energy flux divergence (related to the generation of energy) are shown. In figure 12(*a*), the energy fluxes are calculated from fields containing all wavenumbers, while in figure 12(*b*) truncated fields consisting of an arbitrarily chosen spectral wavenumber band $75 \leqslant k \leqslant 80$ are used. Both plots were obtained by averaging 350 samples over 2400 time-steps of integration during the statistical equilibrium state. During that relatively short period, the large-scale potential-vortical component vortices did not move significantly (as is evident from the well-defined isolated vortices seen even in the time mean shown in figure 12).

Both plots show that regions of strong divergence of inertio-gravity wave energy flux appear to be located in proximity to the large-scale potential-vortical component vortices. The spatial correlation coefficient between these two fields is about 0.47 and 0.60 for figures 12(*a*) and 12(*b*) respectively. This further indicates that the large-

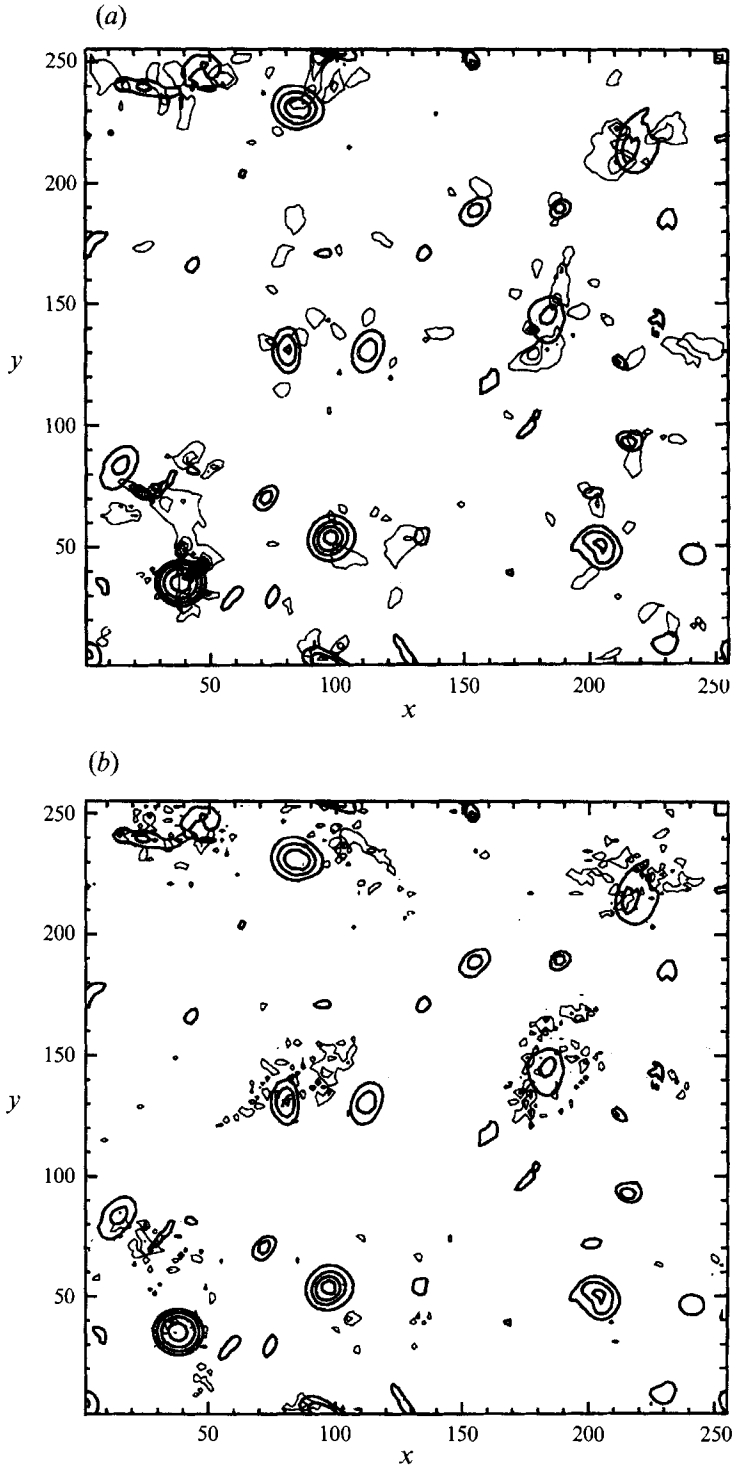

FIGURE 12. Contours of divergence of inertio-gravity wave energy fluxes (thin), and of the absolute value of the potential-vortical component vorticity (heavy): (*a*) and (*b*) are for the energy fluxes in the full and band-passed fields, respectively. The vorticity contour interval is 2×10^{-5} s^{-1} and the minimum contour value plotted is 4×10^{-5} for both panels. In (*a*) the divergence contour interval and minimum value plotted are 1×10^{-6} m s^{-1} and 2×10^{-6} m s^{-1}. In (*b*) the divergence contour interval and minimum value plotted are 3×10^{-9} m s^{-1} and 3×10^{-9} m s^{-1}.

scale potential-vortical component modes are indeed the direct sources of inertio-gravity wave energy. It is interesting that the regions of wave flux divergence are generally found around the edges of the large vortices. Numerous simulations of two-dimensional flow have shown a tendency for the fluid (and the vorticity field itself) near the edge of vortices to be ejected out in filaments that become increasingly stretched out with time. Perhaps in a divergent system it is in such structures that the gradient-wind balance breaks down, leading to the generation of gravity waves. Clearly more work needs to be done to confirm this speculation, but it seems likely that the physical space correlation seen in figure 12 contains valuable information on the nature of the instability of balanced motion in fully developed turbulent flows.

5. Conclusions

In this paper we have investigated the statistical equilibrium dynamics in a forced-dissipative f-plane shallow-water system. We have considered the meteorologically interesting parameter range with both Rossby and Froude numbers $\sim 0.1 - 1$. The detailed dynamics has been analysed by decomposition of the full flow field into a dynamically balanced potential-vortical component and a residual component. The nonlinear decomposition scheme employed was shown to effectively separate the full flow field into slowly evolving motions with properties very similar to those found in the familiar non-divergent system, and higher-frequency motions that behave very much as linear inertio-gravity waves.

The behaviour of the potential-vortical component in the present experiments is strikingly similar to that in purely non-divergent models. In particular, the equilibrium energy spectrum of the potential-vortical component has a logarithmic slope slightly steeper than -3 between the forcing and dissipation ranges. This slope was found to be rather insensitive to the forcing amplitude and rotation rate. Very similar flow statistics were obtained with a quasi-geostrophic shallow-water model run with comparable forcing and dissipation. Detailed analysis of the potential-vortical component showed that the forward (i.e. downscale) enstrophy cascade into any wavenumber is dominated by elongated triads which involve very large-scale modes. This is in agreement with earlier theoretical predictions based on phenomenological turbulence models and with the recent direct calculations of Maltrud & Vallis (1993), but it does contradict the simplest view of the inertial range, i.e. that the cascade into any wavenumber should depend only on components of the flow with similar scales.

Even when not directly forced, a substantial amount of inertio-gravity wave energy can be generated in the system. When the Rossby number exceeds about 0.2, the slope of the inertio-gravity wave spectrum is significantly shallower than that of the balanced motions, so that at high wavenumbers the total energy spectrum is dominated by the inertio-gravity wave component. This behaviour has obvious parallels with the mesoscale spectral regime observed in the atmosphere. It is striking that when parameters roughly appropriate for midlatitude atmospheric flow are employed, the break between the k^{-3} and shallower regimes in the model occurs at wavelengths of a few hundred km, i.e. near the beginning of the mesoscale regime in typical observations. The present results thus demonstrate the possibility of generating a mesoscale regime dominated by gravity waves without invoking direct forcing of the flow at small scales.

No universal shape of the inertio-gravity wave equilibrium spectrum was obtained. Rather the spectrum was found to be highly sensitive to both the forcing amplitude and rotation rate.

In equilibrium, inertio-gravity waves at large scales were shown to gain energy through interactions of inertio-gravity waves with large-scale potential-vortical component modes. This energy is then transferred to dissipation ranges by interactions among inertio-gravity waves themselves. The nonlinear interactions among inertio-gravity waves were found to be extremely broadband in spectral space, in contrast to the interactions among potential-vortical modes. This difference in the nature of the nonlinear interactions is reflected in the behaviour of the equilibrium spectrum as a function of model resolution. As long as the dissipation timescale for the smallest resolved waves is kept constant, the potential-vortical component spectrum was found to be virtually independent of resolution. The inertio-gravity wave energy spectrum, by contrast, was strongly dependent on resolution, suggesting that the simple ∇^8 linear diffusion employed here is not an appropriate subgrid-scale closure for a divergent shallow-water model. This result emphasizes the difficulty in formulating adequate closure schemes for meteorological models that include explicit representation of the motions in the mesoscale regime.

We would like to thank Jeffrey Anderson, Kirk Bryan, Isaac Held, Vitaly Larichev, Jerry Mahlman, Geoffrey Vallis, Tom Warn, Gareth Williams and an anonymous reviewer for helpful discussions and comments.

Appendix A. Definition of nonlinear interaction terms in the full field equations

Using (2.8)–(2.10), (2.1)–(2.3) can be rewritten as

$$\frac{\partial}{\partial t}\nabla^2\psi + \mathscr{J}^{\psi}_{\mathrm{vv}} + \mathscr{J}^{\psi}_{\mathrm{vg}} + \mathscr{J}^{\psi}_{\mathrm{gg}} + f\nabla^2\chi = 0, \tag{A 1}$$

$$\frac{\partial}{\partial t}\nabla^2\chi + \mathscr{J}^{\chi}_{\mathrm{vv}} + \mathscr{J}^{\chi}_{\mathrm{vg}} + \mathscr{J}^{\chi}_{\mathrm{gg}} + \nabla^2(gh - f\psi) = 0, \tag{A 2}$$

$$\frac{\partial h}{\partial t} + \mathscr{J}^{h}_{\mathrm{vv}} + \mathscr{J}^{h}_{\mathrm{vg}} + \mathscr{J}^{h}_{\mathrm{gg}} + H\nabla^2\chi = 0, \tag{A 3}$$

where

$$\mathscr{J}^{\psi}_{\mathrm{vv}} = J(\psi_{\mathrm{v}}, \nabla^2\psi_{\mathrm{v}}) + \nabla\cdot(\nabla^2\psi_{\mathrm{v}}\nabla\chi_{\mathrm{v}}) + \lambda_{\mathrm{o}}^{-2}(\nabla^2 - \lambda_{\mathrm{o}}^{-2})^{-1}J(\psi_{\mathrm{v}}, \nabla^2\psi_{\mathrm{v}}), \tag{A 4}$$

$$\mathscr{J}^{\psi}_{\mathrm{vg}} = J(\psi_{\mathrm{v}}, \nabla^2\psi_{\mathrm{g}}) + J(\psi_{\mathrm{g}}, \nabla^2\psi_{\mathrm{v}}) + \nabla\cdot(\nabla^2\psi_{\mathrm{v}}\nabla\chi_{\mathrm{g}}) + \nabla\cdot(\nabla^2\psi_{\mathrm{g}}\nabla\chi_{\mathrm{v}}) + (\bar{u}\nabla^2\psi_x + \bar{v}\nabla^2\psi_y), \tag{A 5}$$

$$\mathscr{J}^{\psi}_{\mathrm{gg}} = J(\psi_{\mathrm{g}}, \nabla^2\psi_{\mathrm{g}}) + \nabla\cdot(\nabla^2\psi_{\mathrm{g}}\nabla\chi_{\mathrm{g}}), \tag{A 6}$$

$$\mathscr{J}^{\chi}_{\mathrm{vv}} = J(\chi_{\mathrm{v}}, \nabla^2\psi_{\mathrm{v}}) - (\nabla^2\psi_{\mathrm{v}})^2 - (\psi_{\mathrm{v}x}\nabla^2\psi_{\mathrm{v}x} + \psi_{\mathrm{v}y}\nabla^2\psi_{\mathrm{v}y}) + \nabla^2\left[\tfrac{1}{2}(\nabla\psi_{\mathrm{v}}\cdot\nabla\psi_{\mathrm{v}} + \nabla\chi_{\mathrm{v}}\cdot\nabla\chi_{\mathrm{v}}) + J(\psi_{\mathrm{v}}, \chi_{\mathrm{v}})\right] + 2J(\psi_{\mathrm{v}x}, \psi_{\mathrm{v}y}), \tag{A 7}$$

$$\begin{aligned}\mathscr{J}^{\chi}_{\mathrm{vg}} = {} & J(\chi_{\mathrm{g}}, \nabla^2\psi_{\mathrm{v}}) + J(\chi_{\mathrm{v}}, \nabla^2\psi_{\mathrm{g}}) - 2\nabla^2\psi_{\mathrm{v}}\nabla^2\psi_{\mathrm{g}} \\ & -(\psi_{\mathrm{g}x}\nabla^2\psi_{\mathrm{v}x} + \psi_{\mathrm{g}y}\nabla^2\psi_{\mathrm{v}y}) - (\psi_{\mathrm{v}x}\nabla^2\psi_{\mathrm{g}x} + \psi_{\mathrm{v}y}\nabla^2\psi_{\mathrm{g}y}) \\ & +\nabla^2\left[\nabla\psi_{\mathrm{v}}\cdot\nabla\psi_{\mathrm{g}} + \nabla\chi_{\mathrm{v}}\cdot\nabla\chi_{\mathrm{g}} + J(\psi_{\mathrm{v}}, \chi_{\mathrm{g}}) + J(\psi_{\mathrm{g}}, \chi_{\mathrm{v}})\right] \\ & +(\bar{u}\nabla^2\chi_x + \bar{v}\nabla^2\chi_y),\end{aligned} \tag{A 8}$$

$$\mathscr{J}^{\chi}_{\mathrm{gg}} = J(\chi_{\mathrm{g}}, \nabla^2\psi_{\mathrm{g}}) - (\nabla^2\psi_{\mathrm{g}})^2 - (\psi_{\mathrm{g}x}\nabla^2\psi_{\mathrm{g}x} + \psi_{\mathrm{g}y}\nabla^2\psi_{\mathrm{g}y}) + \nabla^2\left[\tfrac{1}{2}(\nabla\psi_{\mathrm{g}}\cdot\nabla\psi_{\mathrm{g}} + \nabla\chi_{\mathrm{g}}\cdot\nabla\chi_{\mathrm{g}}) + J(\psi_{\mathrm{g}}, \chi_{\mathrm{g}})\right], \tag{A 9}$$

$$\mathscr{I}^h_{vv} = -J(\psi_v, h_v) - \nabla\cdot(h_v\nabla\chi_v) - \frac{H}{f\lambda_o^2}(\nabla^2 - \lambda_o^{-2})^{-1}J(\psi_v, \nabla^2\psi_v), \tag{A 10}$$

$$\mathscr{I}^h_{vg} = -J(\psi_v, h_g) - J(\psi_g, h_v) - \nabla\cdot(h_g\nabla\chi_v) - \nabla\cdot(h_v\nabla\chi_g) - (\bar{u}h_x + \bar{v}h_y), \tag{A 11}$$

$$\mathscr{I}^h_{gg} = -J(\psi_g, h_g) - \nabla\cdot(h_g\nabla\chi_g). \tag{A 12}$$

The subscripts and superscripts have the same meanings as in (2.15)–(2.17).

Appendix B. Detailed decomposition of gg interactions

The energy transfer related to $f_a(\boldsymbol{l})$ is assigned as follows where all the nonlinear terms of gg interaction in (2.26) are included:

$$\begin{aligned}
&(-k^{-2}\hat{\mathscr{I}}^{\psi}_{ggy} + (k^2+\lambda_o^{-2})^{-1}\hat{\mathscr{I}}^{\psi_v}_{ggy} + k^{-2}\hat{\mathscr{I}}^{\chi}_{ggx})(-\hat{\psi}^*_{gy} + \hat{\chi}^*_{gx})\\
&+(k^{-2}\hat{\mathscr{I}}^{\psi}_{ggx} - (k^2+\lambda_o^{-2})^{-1}\hat{\mathscr{I}}^{\psi_v}_{ggx} + k^{-2}\hat{\mathscr{I}}^{\chi}_{ggy})(\hat{\psi}^*_{gx} + \hat{\chi}^*_{gy})\\
&+\frac{g}{H}(\hat{\mathscr{I}}^h_{gg} - \frac{f}{g}(k^2+\lambda_o^{-2})^{-1}\hat{\mathscr{I}}^{\psi_v}_{gg})\hat{h}^*_g\\
=\sum_l\{&-k^{-2}[\hat{\psi}_{gx}(\boldsymbol{l})\hat{\zeta}_{gy}(\boldsymbol{k}-\boldsymbol{l}) - \hat{\psi}_{gy}(\boldsymbol{l})\hat{\zeta}_{gx}(\boldsymbol{k}-\boldsymbol{l})\\
&+\hat{\zeta}_{gx}(\boldsymbol{l})\hat{\chi}_{gx}(\boldsymbol{k}-\boldsymbol{l}) + \hat{\zeta}_{gy}\hat{\chi}_{gy}(\boldsymbol{k}-\boldsymbol{l}) + \hat{\zeta}_g(\hat{\chi}_{gxx}(\boldsymbol{k}-\boldsymbol{l}) + \hat{\chi}_{gyy}(\boldsymbol{k}-\boldsymbol{l}))]_y\\
&+k^{-2}[\hat{\chi}_{gx}(\boldsymbol{l})\hat{\zeta}_{gy}(\boldsymbol{k}-\boldsymbol{l}) - \hat{\chi}_{gy}(\boldsymbol{l})\hat{\zeta}_{gx}(\boldsymbol{k}-\boldsymbol{l}) - \hat{\zeta}_g(\boldsymbol{l})\hat{\zeta}_g(\boldsymbol{k}-\boldsymbol{l})\\
&-\hat{\psi}_{gx}(\boldsymbol{l})\hat{\zeta}_{gx}(\boldsymbol{k}-\boldsymbol{l}) - \hat{\psi}_{gy}(\boldsymbol{l})\hat{\zeta}_{gy}(\boldsymbol{k}-\boldsymbol{l}) + \frac{1}{2}(\hat{\psi}_{gx}(\boldsymbol{l})\hat{\psi}_{gx}(\boldsymbol{k}-\boldsymbol{l}) + \hat{\psi}_{gy}(\boldsymbol{l})\hat{\psi}_{gy}(\boldsymbol{k}-\boldsymbol{l})\\
&+\hat{\chi}_{gx}(\boldsymbol{l})\hat{\chi}_{gx}(\boldsymbol{k}-\boldsymbol{l}) + \hat{\chi}_{gy}(\boldsymbol{l})\hat{\chi}_{gy}(\boldsymbol{k}-\boldsymbol{l}) + \hat{\psi}_{gx}(\boldsymbol{l})\hat{\chi}_{gy}(\boldsymbol{k}-\boldsymbol{l}) - \hat{\psi}_{gy}(\boldsymbol{l})\hat{\chi}_{gx}(\boldsymbol{k}-\boldsymbol{l}))_{xx}\\
&+\frac{1}{2}(\hat{\psi}_{gx}(\boldsymbol{l})\hat{\psi}_{gx}(\boldsymbol{k}-\boldsymbol{l}) + \hat{\psi}_{gy}(\boldsymbol{l})\hat{\psi}_{gy}(\boldsymbol{k}-\boldsymbol{l}) + \hat{\chi}_{gx}(\boldsymbol{l})\hat{\chi}_{gx}(\boldsymbol{k}-\boldsymbol{l}) + \hat{\chi}_{gy}(\boldsymbol{l})\hat{\chi}_{gy}(\boldsymbol{k}-\boldsymbol{l})\\
&+\hat{\psi}_{gx}(\boldsymbol{l})\hat{\chi}_{gy}(\boldsymbol{k}-\boldsymbol{l}) - \hat{\psi}_{gy}(\boldsymbol{l})\hat{\chi}_{gx}(\boldsymbol{k}-\boldsymbol{l}))_{yy}]_x\}\times(-\hat{\psi}^*_{gy} + \hat{\chi}^*_{gx})\\
&+\{k^{-2}[\hat{\psi}_{gx}(\boldsymbol{l})\hat{\zeta}_{gy}(\boldsymbol{k}-\boldsymbol{l}) - \hat{\psi}_{gy}(\boldsymbol{l})\hat{\zeta}_{gx}(\boldsymbol{k}-\boldsymbol{l}) + \hat{\zeta}_{gx}(\boldsymbol{l})\hat{\chi}_{gx}(\boldsymbol{k}-\boldsymbol{l}) + \hat{\zeta}_{gy}\hat{\chi}_{gy}(\boldsymbol{k}-\boldsymbol{l})\\
&+\hat{\zeta}_g(\hat{\chi}_{gxx}(\boldsymbol{k}-\boldsymbol{l}) + \hat{\chi}_{gyy}(\boldsymbol{k}-\boldsymbol{l}))]_x\\
&+k^{-2}[\hat{\chi}_{gx}(\boldsymbol{l})\hat{\zeta}_{gy}(\boldsymbol{k}-\boldsymbol{l}) - \hat{\chi}_{gy}(\boldsymbol{l})\hat{\zeta}_{gx}(\boldsymbol{k}-\boldsymbol{l}) - \hat{\zeta}_g(\boldsymbol{l})\hat{\zeta}_g(\boldsymbol{k}-\boldsymbol{l})\\
&-\hat{\psi}_{gx}(\boldsymbol{l})\hat{\zeta}_{gx}(\boldsymbol{k}-\boldsymbol{l}) - \hat{\psi}_{gy}(\boldsymbol{l})\hat{\zeta}_{gy}(\boldsymbol{k}-\boldsymbol{l}) + \frac{1}{2}(\hat{\psi}_{gx}(\boldsymbol{l})\hat{\psi}_{gx}(\boldsymbol{k}-\boldsymbol{l}) + \hat{\psi}_{gy}(\boldsymbol{l})\hat{\psi}_{gy}(\boldsymbol{k}-\boldsymbol{l})\\
&+\hat{\chi}_{gx}(\boldsymbol{l})\hat{\chi}_{gx}(\boldsymbol{k}-\boldsymbol{l}) + \hat{\chi}_{gy}(\boldsymbol{l})\hat{\chi}_{gy}(\boldsymbol{k}-\boldsymbol{l}) + \hat{\psi}_{gx}(\boldsymbol{l})\hat{\chi}_{gy}(\boldsymbol{k}-\boldsymbol{l}) - \hat{\psi}_{gy}(\boldsymbol{l})\hat{\chi}_{gx}(\boldsymbol{k}-\boldsymbol{l}))_{xx}\\
&+\frac{1}{2}(\hat{\psi}_{gx}(\boldsymbol{l})\hat{\psi}_{gx}(\boldsymbol{k}-\boldsymbol{l}) + \hat{\psi}_{gy}(\boldsymbol{l})\hat{\psi}_{gy}(\boldsymbol{k}-\boldsymbol{l}) + \hat{\chi}_{gx}(\boldsymbol{l})\hat{\chi}_{gx}(\boldsymbol{k}-\boldsymbol{l}) + \hat{\chi}_{gy}(\boldsymbol{l})\hat{\chi}_{gy}(\boldsymbol{k}-\boldsymbol{l})\\
&+\hat{\psi}_{gx}(\boldsymbol{l})\hat{\chi}_{gy}(\boldsymbol{k}-\boldsymbol{l}) - \hat{\psi}_{gy}(\boldsymbol{l})\hat{\chi}_{gx}(\boldsymbol{k}-\boldsymbol{l}))_{yy}]_y\}\times(\hat{\psi}^*_{gx} + \hat{\chi}^*_{gy})\\
&+\frac{g}{H}\{\hat{\psi}_{gy}(\boldsymbol{l})\hat{h}_{gx}(\boldsymbol{k}-\boldsymbol{l}) - \hat{\psi}_{gx}(\boldsymbol{l})\hat{h}_{gy}(\boldsymbol{k}-\boldsymbol{l}) - \hat{h}_g(\boldsymbol{l})(\hat{\chi}_{gxx}(\boldsymbol{k}-\boldsymbol{l}) + \hat{\chi}_{gyy}(\boldsymbol{k}-\boldsymbol{l}))\\
&-\hat{h}_{gx}(\boldsymbol{l})\hat{\chi}_{gx}(\boldsymbol{k}-\boldsymbol{l}) - \hat{h}_{gy}(\boldsymbol{l})\hat{\chi}_{gy}(\boldsymbol{k}-\boldsymbol{l})\}\hat{h}^*_g,
\end{aligned} \tag{B 1}$$

where $\zeta = \nabla^2\psi$. To obtain the transfer related to $f_b(\boldsymbol{l})$, just simply exchange $(\boldsymbol{l})$ and $(\boldsymbol{k}-\boldsymbol{l})$.

REFERENCES

BASDEVANT, C., LEGRAS, B., SADOURNY, R. & BELAND, M. 1981 A study of barotropic model flows: intermittency, waves and predictability. *J. Atmos. Sci.* **38**, 2305–2326.

BASDEVANT, C., LESIEUR, M. & SADOURNY, R. 1978 Subgrid-scale modeling of enstrophy transfer in two-dimensional turbulence. *J. Atmos. Sci.* **35**, 1028–1042.

BOER, G. J. & SHEPHERD, T. G. 1983 Large-scale two-dimensional turbulence in the atmosphere. *J. Atmos. Sci.* **40**, 164–183.

FARGE, M. & LACARRA, J. F. 1988 The numerical modelling of shallow-water equations. *J. Méc. Théor. Appl. Special Issue Suppl.* **7**, 63–86.

FARGE, M. & SADOURNY, R. 1989 Wave-vortex dynamics in rotating shallow water. *J. Fluid Mech.* **206**, 433–462 (referred to herein as FS).

FORNBERG, B. 1977 A numerical study of two-dimensional turbulence. *J. Comput. Phys.* **25**, 1–31.

GAGE, K. S. & NASTROM, G. D. 1986 Theoretical interpretation of atmospheric wavenumber spectra of wind and temperature observed by commercial aircraft during GASP. *J. Atmos. Sci.* **43**, 729–740.

HOYER, J. M. & SADOURNY, R. 1982 Closure modeling of fully developed baroclinic instability. *J. Atmos. Sci.* **39**, 707–721.

KRAICHNAN, R. H. 1967 Inertial ranges in two-dimensional turbulence. *Phys. Fluids* **10**, 1417–1423.

KRAICHNAN, R. H. 1975 Statistical dynamics of two-dimensional flow. *J. Fluid Mech.* **67**, 155–175.

LEGRAS, B., SANTANGELO, P. & BENZI, R. 1988 High resolution numerical experiments for forced two-dimensional turbulence. *Europhys. Lett.*, **5**, 37–42.

LILLY, D. K. 1972 Numerical simulation studies of two-dimensional turbulence. *Geophys. Fluid Dyn.* **3**, 289–319.

LILLY, D. K. 1983 Stratified turbulence and the mesoscale variability of the atmosphere. *J. Atmos. Sci.* **40**, 749–761.

LORENZ, E. N. 1980 Attractor sets and quasi-geostrophic equilibrium. *J. Atmos. Sci.* **37**, 1685–1699.

MALTRUD, M. E. & VALLIS, G. K. 1991 Energy spectra and coherent structures in forced two-dimensional and beta-plane turbulence. *J. Fluid Mech.* **228**, 321–342.

MALTRUD, M. E. & VALLIS, G. K. 1993 Energy and enstrophy transfer in numerical simulations of two-dimensional turbulence. *Phys. Fluids* **5**, 1760–1775.

MCWILLIAMS, J. C. 1984 The emergence of coherent vortices in turbulent flow. *J. Fluid Mech.* **146**, 21–43.

NASTROM, G. D. & GAGE, K. S. 1985 A climatology of atmospheric wavenumber spectra observed by commercial aircraft. *J. Atmos. Sci.* **42**, 950–960.

OHKITANI, K. & KIDA, S. 1992 Triad interactions in a forced turbulence. *Phys. Fluids* A **4**, 794–802.

POLVANI, L. M., MCWILLIAMS, J. C., SPALL, M. A. & FORD, R. 1994 The coherent structures of shallow-water turbulence: deformation-radius effects, cyclone/anticyclone asymmetry and gravity-wave generation. *Chaos* (in press).

POUQUET, A., LESIEUR, M., ANDRE, J. C. & BASDEVANT, C. 1975 Evolution of high Reynolds number two-dimensional turbulence. *J. Fluid Mech.* **72**, 305–319.

SPALL, M. & MCWILLIAMS, J. C. 1992 Rotational and gravitational influences on the degree of balance in the shallow-water equations. *Geophys. Astrophys. Fluid Dyn.* **64**, 1–29.

STRAHAN, S. & MAHLMAN, J. D. 1994 Evaluation of the GFDL "SKYHI" general circulation model using aircraft N_2O measurements: II Tracer variability and diabatic meridional circulation. *J. Geophys. Res.* **99**, 10319–10332.

WARN, T. 1986 Statistical mechanical equilibria of the shallow-water equations. *Tellus* **38A**, 1–11.

YUAN, L. 1993 Statistical equilibrium dynamics in a forced-dissipative shallow-water system. PhD thesis, Princeton University, Princeton, New Jersey.